

1 **Application of the Pseudo-Global Warming Approach**
2 **in a Kilometer-Resolution Climate Simulation of the**
3 **Tropics**

4 **Christoph Heim¹, David Leutwyler¹, Christoph Schär¹**

5 ¹Institute for Atmospheric and Climate Science, ETH Zurich, Zürich, Switzerland

6 **Key Points:**

- 7 • We perform a kilometer-resolution climate simulation over the tropical Atlantic
8 for current and future climate conditions using the PGW approach
9 • We find an accurate representation of the annual cycle of shallow cumulus clouds
10 and a realistic structure of the ITCZ, without double ITCZ
11 • The ITCZ intensifies in a warming climate while the narrowing typically seen in
12 GCMs is not visible

13 **Abstract**

14 Clouds over tropical oceans are an important factor in Earth's response to increased green-
 15 house gas concentrations, but their representation in climate models is challenging due
 16 to the small-scale nature of the involved convective processes.

17 We perform two 4-year-long simulations at kilometer-resolution (3.3 km horizontal grid
 18 spacing) with the limited-area model COSMO over the tropical Atlantic on a $9000 \times 7000 \text{ km}^2$
 19 domain: A control simulation under current climate conditions driven by the ERA5 re-
 20 analysis, and a climate change scenario simulation using the Pseudo-Global Warming
 21 (PGW) approach. We compare these results to the changes projected in the CMIP6 sce-
 22 nario ensemble.

23 We find a good representation of the annual cycle of albedo, in particular for trade-wind
 24 clouds, even compared to the ERA5 reanalysis. Also, the vertical structure and annual
 25 cycle of the marine intertropical convergence zone (ITCZ) is accurately simulated, and
 26 the simulation does not suffer from the double ITCZ problem commonly present in global
 27 climate models (GCMs). The ITCZ responds to warming through a vertical extension
 28 and intensification primarily at high levels, as well as a slight southward extension of the
 29 annual mean ITCZ, while the narrowing typically seen in GCMs is not visible.

30 **1 Introduction**

31 Clouds over tropical oceans are among the most uncertain factors controlling Earth's
 32 temperature response to anthropogenic greenhouse gas emissions (Forster et al., 2021).
 33 They form along the branches of the Hadley circulation (HC, e.g. Held & Hou, 1980),
 34 for instance, in the form of deep convection at the intertropical convergence zone (ITCZ)
 35 (Waliser & Gautier, 1993) and shallow convection in the marine boundary layer (MBL)
 36 in the Trades (e.g. Stevens, 2007; Wood, 2012; Vial et al., 2017). Tropical clouds have
 37 the potential for a strong radiative feedback in a warming climate (Bony & Dufresne,
 38 2005; Zelinka et al., 2016). Yet, their evolution with climate change is uncertain (e.g. Brether-
 39 ton, 2015), making them a prime focus of current climate change research.

40 Model intercomparison projects of global climate models (GCMs) such as the fifth
 41 or sixth phase of the Coupled Model Intercomparison Project (CMIP5, CMIP6, Taylor
 42 et al., 2012; Eyring et al., 2016) allow for an assessment of the magnitude and inter-model
 43 variability of cloud changes in a large ensemble of state-of-the-art GCMs. With respect

44 to tropical deep convection at the ITCZ, many GCMs project that the upper part of the
45 clouds (i.e. the anvils) will rise in a warming atmosphere and remain at approximately
46 the same temperature, according to the fixed anvil temperature (FAT) hypothesis (Hartmann
47 & Larson, 2002). As the anvils rise, they find themselves in a more stable environment
48 which reduces the anvil cloud fraction according to the stability iris hypothesis (Bony
49 et al., 2016). There is observational evidence supporting these hypotheses (Saint-Lu et
50 al., 2020). High-resolution simulations in aqua-planet and slab-ocean configuration mostly
51 reproduce this result of GCMs (Wing et al., 2020), even though there are exceptions (Satoh
52 et al., 2012; Singh & O’Gorman, 2015; Ohno & Satoh, 2018).

53 GCMs also project a narrowing of the annual mean ITCZ with stronger convec-
54 tive ascent near the equator (Huang et al., 2013; Byrne & Schneider, 2016; Byrne et al.,
55 2018), and a drying and widening of the subtropics, which together have been illustra-
56 tively termed the ”deep-tropics squeeze” (Lau & Kim, 2015). These projected changes
57 of tropical deep-convection are statistically robust among GCMs (Lau & Kim, 2015), even
58 though a non-negligible amount of models projects ITCZ changes of opposite sign (Byrne
59 et al., 2018). Yet GCMs do not agree on the representation of the ITCZ under current
60 climate conditions, for example, many models exert a double ITCZ structure (Mechoso
61 et al., 1995; Zhang et al., 2019). While observations show one single annual mean ma-
62 rine ITCZ rain band north of the equator, many GCMs simulate an additional rain band
63 south of the equator at certain locations and seasons. This so-called ”double ITCZ prob-
64 lem” has existed for more than two decades (e.g. Fiedler et al., 2020) and is thought to
65 be linked, among other factors, to air-sea interaction (e.g. Lin, 2007; Li & Xie, 2014) and
66 aspects of convective parameterizations (e.g. Lin, 2007; Bellucci et al., 2010; Song & Zhang,
67 2018). The narrowing and intensification of the convective regions in the deep tropics
68 in a warming climate found in GCMs is supported by observations (Wodzicki & Rapp,
69 2016; Byrne et al., 2018) and thermodynamic arguments (Jenney et al., 2020; Lau et al.,
70 2020). However, it has been argued that the observed narrowing of the ITCZ refers to
71 the width of the seasonal ITCZ band, while the deep-tropics squeeze is evident in the
72 width of the annual-mean zonal-mean tropical ascent region (Zhou et al., 2020). No clear
73 signal of a reduced mid-cloud fraction with warming was found in high-resolution sim-
74 ulations in aqua-planet configurations (Wing et al., 2020). Yet, aqua-planet configura-
75 tions show a large degree of idealization compared to the real world. Comparably lit-

76 tle is known about changes in the structure of the ITCZ from high-resolution climate sim-
77 ulations in real-world application (e.g. Satoh et al., 2012; Tsushima et al., 2014).

78 With respect to tropical low cloud changes, GCMs overall project a reduction of
79 the low-cloud albedo, but the inter-model spread is much larger than in projections of
80 deep convection (e.g. Zelinka et al., 2017; Vial et al., 2017). Also, there is a notorious
81 negative cloud bias in subtropical low-cloud regions in GCMs (e.g. Noda & Satoh, 2014;
82 Kawai & Shige, 2020). Large-eddy simulations (LES) show a more consistent climate change
83 response of low clouds (e.g. Blossey et al., 2013), but given their small domain sizes and
84 idealized setups, generalization of LES results to the entire planet introduces new un-
85 certainties.

86 The fundamental problem behind the representation of convective clouds in GCMs
87 is that a high horizontal and vertical resolution is required to resolve the small-scale con-
88 vective circulations that drive clouds. Convective circulations represent the primary mode
89 of vertical transport in the tropical atmosphere. If unresolved, these circulations, the clouds,
90 as well as the vertical transport of heat and moisture associated with them have to be
91 represented by convective parameterization schemes (e.g. Kawai & Shige, 2020). These
92 schemes introduce substantial uncertainty in the simulation of deep-convective clouds
93 (Suhas & Zhang, 2015), low-level clouds (Vial et al., 2016), and in how these clouds re-
94 spond to climate change (Sherwood et al., 2014; Vial et al., 2017). With higher model
95 resolution, convective parameterizations become less important and can eventually be
96 switched off, which reduces the degree of parameterization and allows for a model for-
97 mulation closer to physical first principles. For deep convective clouds, this threshold is
98 reached at kilometer-resolution (Prein et al., 2015) which is why kilometer-resolution cli-
99 mate simulations are increasingly considered a major milestone towards more confident
100 climate projections (e.g. Schneider et al., 2017; Satoh et al., 2019; Stevens et al., 2020;
101 Schär et al., 2020). Precipitation statistics in the deep tropics have been found to be largely
102 improved at kilometer-resolution compared to coarser models (Klocke et al., 2017; Stevens
103 et al., 2020; Hohenegger et al., 2020).

104 Global kilometer-resolution multi-year climate simulations are not yet feasible due
105 to computational cost (Schär et al., 2020), although rapid progress is evident (e.g. Satoh
106 et al., 2012, 2019; Stevens et al., 2019). Instead, multi-year kilometer-resolution simu-
107 lations are typically run on limited-area domains using boundary conditions from reanal-

ysis data sets for evaluation runs (e.g. Ban et al., 2021), and from GCMs for climate change scenario simulations (e.g. Pichelli et al., 2021). Usually, a historical control simulation and a future scenario simulation are compared to extract the climate change signal. An alternative to this dynamical downscaling approach is the pseudo-global warming (PGW) approach (Adachi & Tomita, 2020; Brogli et al., 2022) in which reanalysis boundary conditions are used for both the control and the scenario simulation. The climate change signal is obtained by imposing large-scale changes in the climate system on the reanalysis boundary fields of the scenario simulation. Doing so has the advantage that the biases from the historical GCM run do not enter the limited-area simulation, and that relatively short simulation periods can be used (Brogli et al., 2022). The PGW approach has extensively been applied in the mid-latitudes (Schär et al., 1996; Wu & Lynch, 2000; Sato et al., 2007; Rasmussen et al., 2011; Kröner et al., 2017; Brogli et al., 2019). We are aware of applications in the subtropics (Chen et al., 2020; Nakamura & Mäll, 2021), but to our knowledge, this study represents the first application of a PGW simulation at kilometer-resolution covering the full extent of the HC including the deep tropics.

We run a 4-year-long limited-area atmospheric simulation at 3.3 km resolution over the tropical Atlantic with the goal to (i) evaluate how well the tropical climate and the associated distribution of clouds are represented in a kilometer-resolution atmospheric model, and (ii) compare the climate change response of the HC in terms of its structure, dynamics and clouds to the projections from the CMIP6 models. In a subsequent paper, a systematic analysis of the ensuing radiative feedbacks in this simulation will be presented. The following Section describes the modelling framework. Section 3 presents the results which are discussed in Section 4 and concluded in Section 5.

2 Materials and Methods

2.1 Experimental Setup

The limited-area model COSMO (see Section 2.3) is used in two 4-year-long simulations. The first one (CTRL) serves as a control simulation and represents current climate conditions. It is initialized and driven at the boundaries by the European Center for Medium Range Weather Forecast (ECMWF) ERA5 Re-Analysis (Hersbach et al., 2020). CTRL is used to evaluate the COSMO model against observations, and serves as a baseline for comparison with the second simulation. The second simulation is a cli-

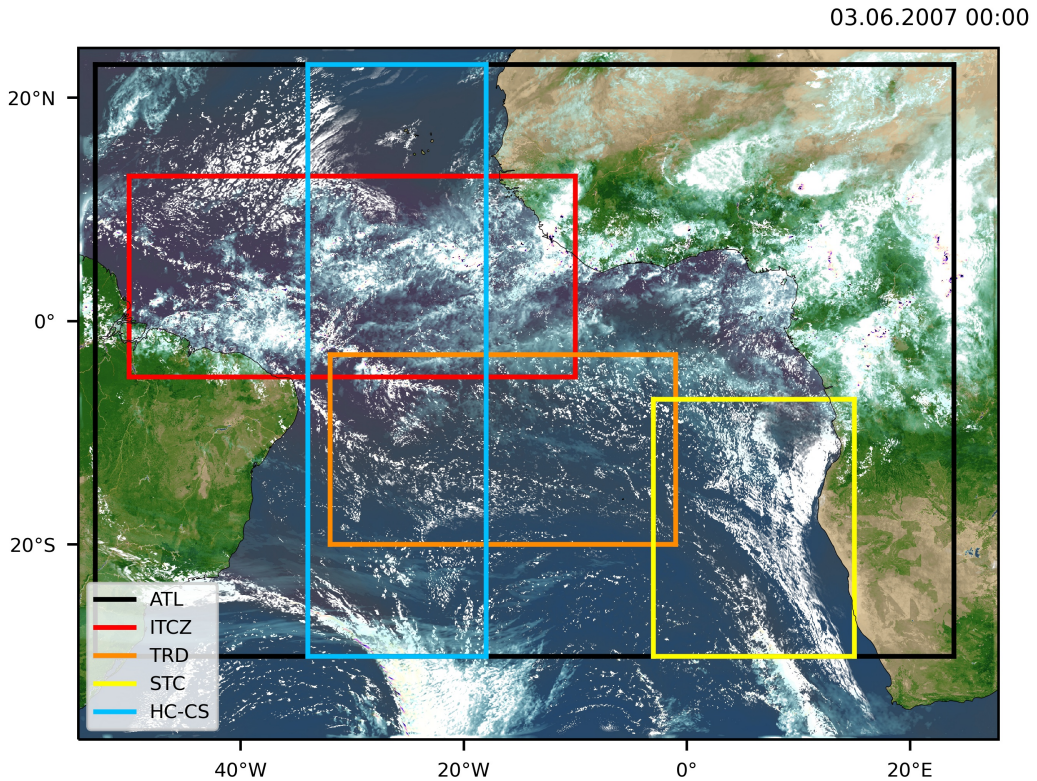


Figure 1. Simulation visualization and analysis domains. The COSMO simulations are run on the entire domain shown and the rectangles indicate different analysis domains. ATL covers the South Atlantic deep tropics and subtropics (30°S - 23°N). The three subdomains ITCZ, TRD and STC comprise the regions of the three major tropical marine cloud regimes (deep convection at the ITCZ, trade-wind cumulus and stratocumulus). The HC-CS is used to compute altitude-latitude cross-sections to visualize the structure of the Hadley cell.

139 mate change scenario simulation (PGW) obtained with the pseudo-global warming ap-
 140 proach (see Section 2.2).

141 Both, CTRL and PGW simulations are initialized on August 1, 2006 (for details
 142 on the initialization see below) and the analysis is done for the years 2007-2010 and fo-
 143 cused on five geographic regions (Fig. 1). The analysis period is too short to fully av-
 144 erage out inter-annual variability. The effect of this is quantified in Section 3. The sim-
 145 ulation domain covers 37.5° S - 24.5° N and 54.5° W - 28.0° E and consists of $2750 \times 2065 \times 60$
 146 grid points at $0.03^{\circ} / 3.3$ km resolution, integrated with a time step of 25 seconds. The
 147 vertical grid stretches to an altitude of 30 km with a resolution of about 20 m near the
 148 surface, 500 m at 5 km altitude, and 1.5 km at the model top. The domain covers the deep-
 149 tropical and parts of the subtropical Atlantic (Fig. 1) encompassing the full southern hemi-
 150 spheric branch of the HC. Although the focus lies on the Atlantic, the simulation domain
 151 includes parts of Africa and South America to enable interaction between marine and
 152 continental areas for instance through Monsoon circulations or the African easterly waves.

153 2.2 Pseudo-Global Warming Approach

154 The initial and boundary conditions of the PGW simulation are obtained follow-
 155 ing Brogli et al. (2022) by adding the mean climate change signal (so-called climate deltas)
 156 for temperature, relative humidity, horizontal wind, and surface temperature to the ERA5
 157 boundary conditions of the CTRL simulation period. The climate deltas are a function
 158 of latitude, longitude, pressure and month, and represent the mean annual cycle of the
 159 spatial change pattern between two climate states, i.e. here between a historical and a
 160 future scenario climatology. Note that, apart from the model initialization, the climate
 161 deltas are only applied at the lateral boundary conditions of the limited-area model, and
 162 at the surface for SST. The change signal PGW–CTRL in the interior of the domain
 163 is thus a model-internal response to the forcing applied at the boundaries.

164 The climate deltas are computed from the CMIP6 output of the MPI-ESM1-2-HR
 165 model (von Storch et al., 2017) as the difference between the Intergovernmental Panel
 166 on Climate Change (IPCC) SSP5-8.5 scenario (Kriegler et al., 2017) simulation during
 167 2070 - 2099 and the CMIP6 historical simulation during 1985 - 2014. The output of the
 168 MPI-ESM is obtained as daily mean values from the CMIP6 output group CFday and
 169 aggregated into monthly means. Since this output group was intended for the Cloud Feed-

back Model Intercomparison Project (Webb et al., 2017) it is provided on the native vertical grid of the MPI-ESM model, and hence at fine vertical resolution. Fine resolution is desirable to accurately represent the difference in warming across the trade-wind inversion (see Brogli et al., 2022, Fig. 4 and corresponding discussion). The obtained changes are displayed in the supplemental information (Figs. S1-4).

The monthly mean climate deltas are then linearly interpolated to the grid and time of the ERA5 boundary files of the CTRL simulation where the deltas are added to obtain the boundary files of the PGW simulation. After modifying temperature and relative humidity, the pressure field is adjusted to restore the hydrostatic balance. The corresponding changes in cloud and precipitation quickly adjust to the new thermodynamic environment within the model domain, and are thus not otherwise accounted for in the PGW methodology. The change of the soil temperature is computed based on the surface temperature climate delta assuming an exponential decay of the annual cycle signal with depth. Initial soil moisture is not modified and taken from the CTRL simulation (5 months before the analysis period begins). Greenhouse gas concentrations are held fixed during the simulation and set to 530 ppm CO₂-eq during CTRL and 1100 ppm CO₂-eq during PGW consistent with the SSP5-8.5 scenario. Aerosols are identical in CTRL and PGW following the Tegen et al. (1997) climatology. Even though biomass burning over Africa is a significant source of aerosol over the Atlantic (Zuidema et al., 2016), the change of aerosol loading between CTRL and PGW is neglected here for simplicity. The same is the case for ozone.

2.3 COSMO Model

The COSMO model is a fully compressible non-hydrostatic atmospheric model originally developed as a numerical weather prediction model (Baldauf et al., 2011) and later evolved into a regional climate model (Rockel et al., 2008). Here a COSMO version capable of exploiting Graphics Processing Units is employed (Fuhrer et al., 2014; Leutwyler et al., 2016). This version of COSMO has been extensively validated in kilometre-scale configurations including a 10-year-long reanalysis-driven simulation over Europe (Leutwyler et al., 2017), validation of clouds (Hentgen et al., 2019), and surface winds (Belušić et al., 2018). The model discretizes the horizontal and vertical dimensions on a rotated latitude-longitude grid and a generalised Gal-Chen coordinate, respectively. The model equations are integrated in time with a split-explicit third-order Runge-Kutta scheme (Klemp &

202 Wilhelmson, 1978; Wicker & Skamarock, 2002; Baldauf et al., 2011). Horizontal advection
 203 is treated with a fifth-order advection scheme except for moist quantities which are
 204 integrated using a positive-definite second-order scheme (Bott, 1989). The upper bound-
 205 ary is treated following (Klemp & Durran, 1983) and no relaxation of the model top to-
 206 wards the boundary files is performed.

207 Radiative transfer is computed following the δ -two-stream approach after Ritter
 208 and Geleyn (1992). The subgrid-scale vertical turbulent fluxes are parameterized with
 209 a TKE-based model (Raschendorfer, 2001). Cloud microphysics is parameterized using
 210 the single-moment bulk scheme after Reinhardt and Seifert (2006). The parameteriza-
 211 tions for deep and shallow convection are switched off as this was previously found to
 212 give a reasonable representation of clouds in the COSMO model at kilometer-resolution
 213 (Vergara-Temprado et al., 2020; Heim et al., 2021). At the surface, the second-generation
 214 land-surface model TERRA_ML (Heise et al., 2003) with the groundwater-runoff scheme
 215 after Schlemmer et al. (2018) is used on land grid points.

216 Soil moisture profiles are initialised based on a 12-year-long soil spin up COSMO
 217 simulation at 24 km grid spacing. The resulting soil moisture conditions serve as initial
 218 condition for a 5-month-long spin up at full (3.3 km) resolution, initialized on August
 219 1, 2006 (for CTRL and PGW). Over ocean grid points, sea-surface temperature is read
 220 in from the surface boundary fields. Lateral and surface boundary fields are updated ev-
 221 ery three hours. A number of empirical model parameters are adjusted to improve the
 222 representation of low clouds in comparison to previous simulations over the extratrop-
 223 ics: The vertical turbulent length scale is set to 200 m. The minimum threshold for eddy-
 224 diffusivity for heat and momentum under stable conditions are set to $0.25 \text{ m}^2 \text{ s}^{-1}$ (see
 225 Possner et al. (2014) for more details about these parameters).

226 2.4 Data Sources

227 2.4.1 CMIP6 Models

228 The change signal between the future and the historical climate in COSMO is ob-
 229 tained by taking the difference between the PGW and the CTRL simulation. To put this

230 into perspective, the change signal of the ensemble mean of 26 CMIP6 models¹, here-
 231 after referred to as CMIP6-EM, is computed as the difference between the SSP5-8.5 ex-
 232 periment during 2070-2099 (SCEN), and the historical experiment during 1985-2014 (HIST).
 233 SCEN–HIST is thus consistent with (and in the case of the MPI-ESM model equiva-
 234 lant to) the climate delta of the PGW simulation. The CMIP6-EM is computed using
 235 output of the Amon group, thus with monthly frequency and on 11 pressure levels be-
 236 low 100 hPa. One exception is the cloud fraction which is provided on the native verti-
 237 cal grid. All analyses are performed in geometric altitude space, and the CMIP6 data
 238 is vertically interpolated on a z-coordinate.

239 2.4.2 *Observational Data Sets*

240 The following observational data sets are used to evaluate the simulations:

- 241 • The Clouds and the Earth’s Radiant Energy System (CERES) Energy Balanced
 242 and Filled (EBAF) Top-of-Atmosphere (TOA) Edition-4.0 Data Product (Loeb
 243 et al., 2018) provides monthly values of TOA radiation at 1° horizontal resolution.
- 244 • The Satellite Application Facility on Climate Monitoring (CM SAF) TOA radi-
 245 ation (Clerbaux et al., 2013), based on the Geostationary Earth Radiation Bud-
 246 get (GERB) instrument, provides monthly values of TOA radiation at 45 km hor-
 247 izontal resolution.
- 248 • The global Precipitation Measurement (GPM) Integrated Multi-satellitE Retrievals
 249 for GPM (IMERG) data set (Huffman et al., 2019): provides precipitation obser-
 250 vations at daily frequency and 0.1° horizontal resolution.
- 251 • The ERA5 reanalysis (Hersbach et al., 2020) is a gridded reanalysis data set. It
 252 is obtained from the CDS data store (Copernicus Climate Change Service (C3S),
 253 2017) and used at 3-hourly frequency and 0.25° horizontal resolution.

1

¹ The analysed models include: ACCESS-CM2, ACCESS-ESM1-5, CAMS-CSM1-0, CanESM5, CESM2, CESM2-WACCM, CMCC-CM2-SR5, CMCC-ESM2, CNRM-CM6-1, CNRM-ESM2-1, E3SM-1-1, FGOALS-f3-L, FGOALS-g3, GFDL-CM4, GFDL-ESM4, GISS-E2-1-G, HadGEM3-GC31-LL, MIROC6, MIROC-ES2L, MPI-ESM1-2-HR, MPI-ESM1-2-LR, MRI-ESM2-0, NorESM2-LM, NorESM2-MM, TaiESM1, UKESM1-0-LL

254 **3 Results**

255 We start by looking at a cloud visualization to provide an overview of the cloud
 256 phenomena occurring within the domain. Figure 2 shows snapshots during boreal sum-
 257 mer (top) and winter (bottom). The variety of shapes and scales of tropical cloud phe-
 258 nomena and their representation in the model is remarkable. We list some of the key phe-
 259 nomena in order of decreasing size and show close-up views of them in the small pan-
 260 els (i)-(vi): (i) A mid-latitude frontal system moving eastward across the southern sub-
 261 tropical Atlantic. Such extra-tropical disturbances can reach far into the southern At-
 262 lantic subtropics during boreal summer and alter the properties of the atmosphere and
 263 subsequent formation of MBL clouds (e.g. Schulz et al., 2021). (ii) to the North of the
 264 domain, a tropical cyclone with multiple rain bands has formed and makes its way to-
 265 wards north-west. (iii) Large mesoscale convective systems travelling westward are pro-
 266 ducing heavy rainfall over the African tropical belt. (iv) Deep convection at the marine
 267 ITCZ. (v) The vast region of the Namibian stratocumulus decks (visible in both pan-
 268 els, but with larger extent during boreal winter). Finally, the stratocumulus topped MBL
 269 transitioning into (vi) the trade-wind-cumulus topped MBL on its way towards the deep
 270 tropics. Hereby, different modes of mesoscale cloud aggregation are producing regional
 271 differences in cloud cover.

272 The horizontal and vertical circulations underlying the clouds shown in Fig. 2 – from
 273 the large-scale tropical overturning HC down to small-scale convective MBL circulations
 274 – are all represented explicitly on the model grid, even though many of the circulation
 275 features are resolved only at the coarse end of the spectrum. In the following section,
 276 we are going to evaluate the simulation and compare it to the CMIP6 historical runs.

277 **3.1 Evaluation of the CTRL Simulation**

278 We start the evaluation at the large-scale with the analysis of the meridional struc-
 279 ture of the HC. Afterwards, we look at the spatial structure and annual cycle of indi-
 280 vidual cloud regimes.

281 ***3.1.1 The Hadley Cell***

282 Figure 3 shows the meridional distribution of clouds and surface precipitation along
 283 the HC-CS domain for the annual mean as well as for the 3-month-periods with south-

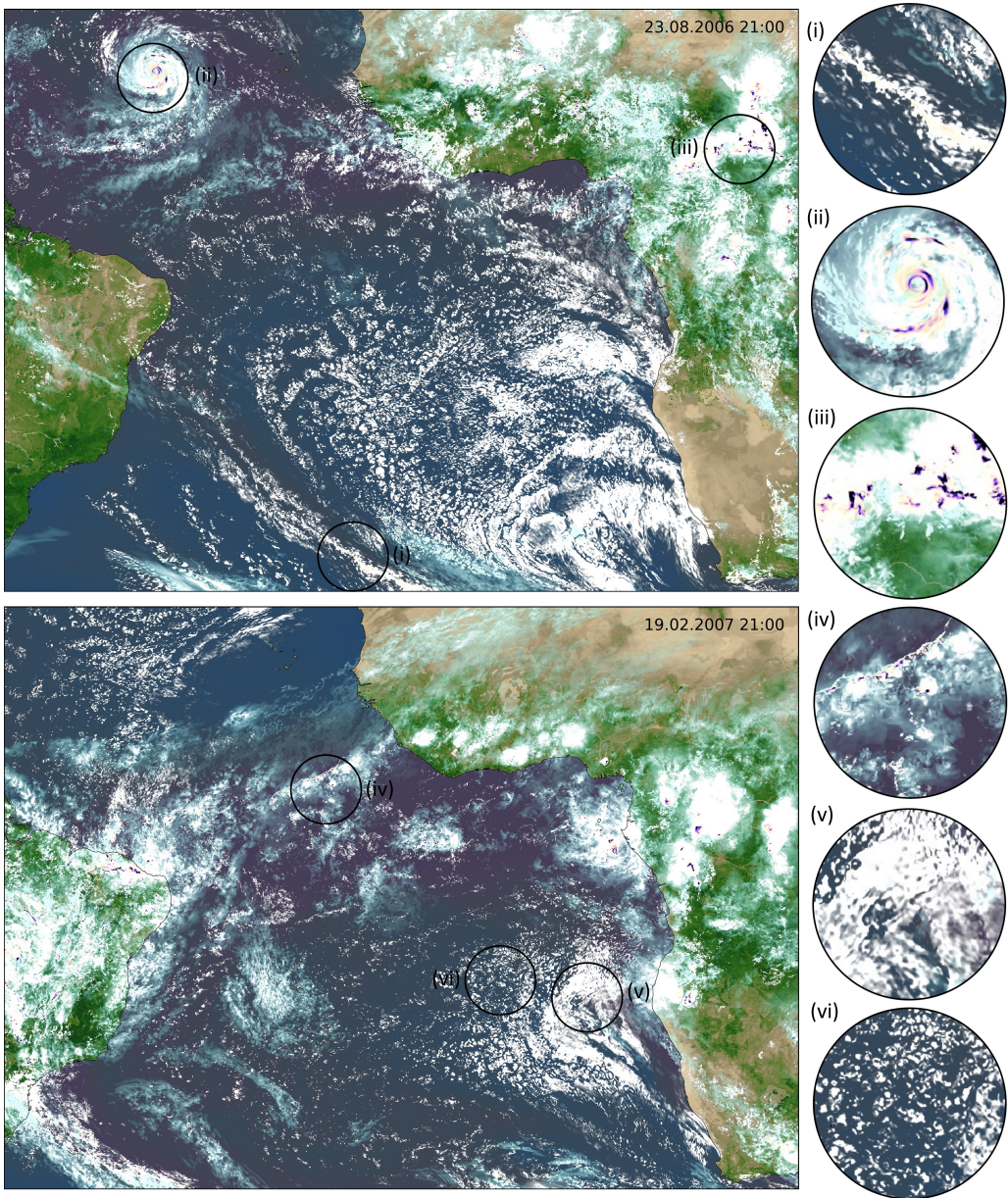


Figure 2. Snapshots of the CTRL simulation obtained during boreal summer on 23.08.2006 21:00 UTC (top) and winter on 19.02.2007 21:00 UTC (bottom). The visualization shows atmospheric cloud liquid and ice water content in white and light-blue-to-white colors, respectively, as well as surface precipitation in yellow-to-blue colors. Areas of high atmospheric water vapor content over oceans are visualized using purple shading. The land surface is rendered based on the model surface albedo and vegetation types, with a desert-to-green color gradient that is modulated by the soil moisture content to imitate the seasonal cycle of vegetation density. The panels on the right-hand side show close-up views of (i) a mid-latitude frontal system, (ii) a tropical cyclone, (iii) a mesoscale convective system, (iv) deep convection at the marine ITCZ, (v) marine stratocumulus clouds, (vi) marine shallow cumulus (or trade-wind cumulus) clouds. An animation of this visualization can be obtained via <https://doi.org/10.3929/ethz-b-000568941>.

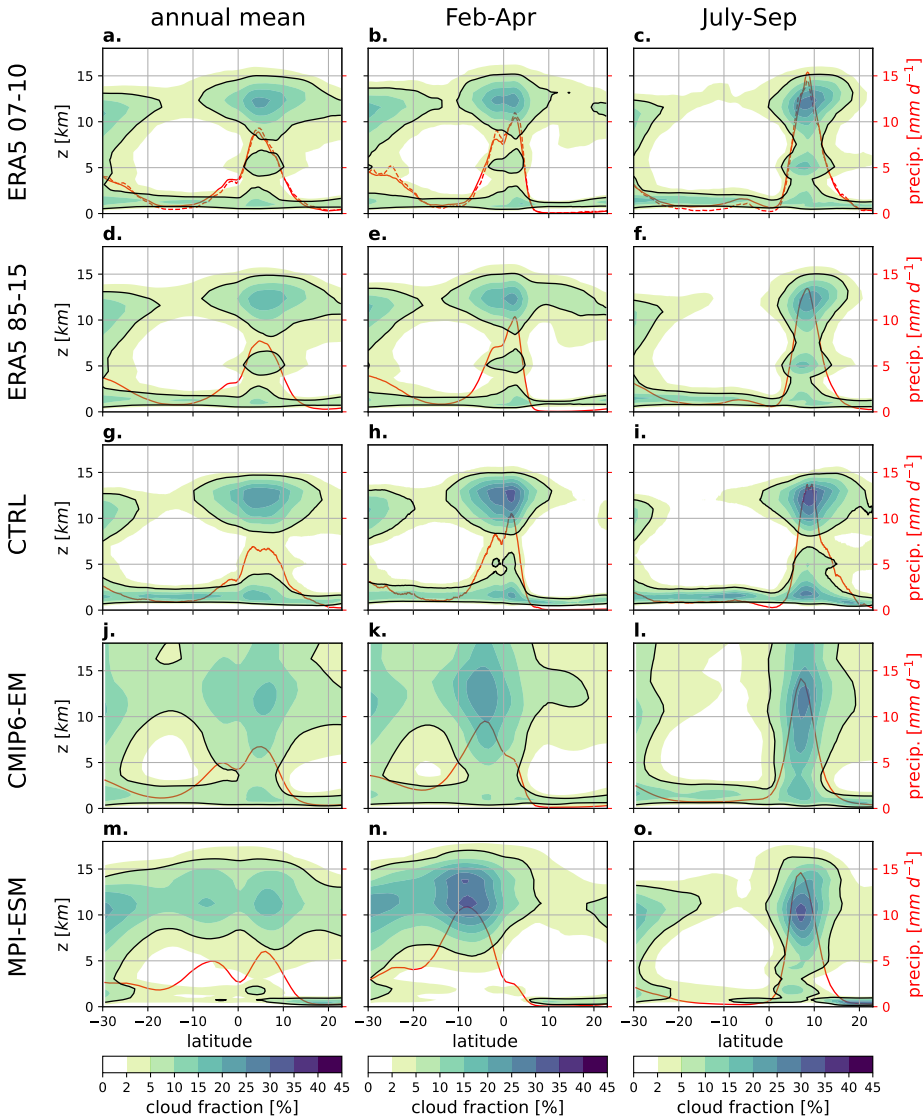


Figure 3. Altitude-latitudinal cross-sections of the cloud fraction [%] averaged along the longitudes of the HC-CS domain. The black contour lines denote the 5% cloud fraction level. The solid red lines show surface precipitation [mm d^{-1}]. The corresponding y-axis is located on the right-hand side of the panels. The panels show (a-c) ERA5 with the same period as the CTRL simulation (2007-2010), (d-f) an extended period of ERA5 corresponding to HIST (1985-2014), (g-i) CTRL (2007-2010), (j-l) CMIP6-EM HIST (1985-2014), and (m-o) MPI-ESM HIST (1985-2014). The three columns represent multi-year averages (left panels) during the entire year, as well as (center panels) during February–April and (right panels) July–September when the marine ITCZ reaches its southernmost and northernmost extent, respectively. The cloud fraction is obtained from the respective model output, except for COSMO where grid points with a specific cloud liquid plus ice water content $\geq 0.01 \text{ g m}^{-3}$ are considered cloudy while the remaining grid points are considered cloud-free. As a complementary reference observation, GPM IMERG precipitation is shown as a red dashed line in panels (a-c).

ernmost (February-April) and northernmost (July-September) extent of the marine ITCZ.
 The ERA5 record (Fig. 3a-c) indicates that the annual mean cloud fraction and precipitation have their peak at 4°N. The peak shifts to 8°N during boreal summer, and splits into a primary peak persisting at 3°N, and a secondary peak at about 2°S during boreal winter. Comparing the 4-year-long (Fig. 3a-c) and the 30-year-long (Fig. 3d-f) ERA5 cross-sections shows that the climatological distributions of cloud and precipitation are well represented by the 4-year-long simulation period used in CTRL (see Section 2.1). The comparison of surface precipitation between ERA5 and GPM IMERG indicates a close agreement between these two reference data sets (Fig. 3a-c).

The zonal mean precipitation is well reproduced in CTRL with respect to ERA5 with the exception of a slightly underestimated annual mean peak (Fig. 3g-i). The CMIP6-EM captures the northward shift of the ITCZ during boreal summer, but largely overestimates the boreal winter secondary peak in the southern hemisphere (Fig. 3j-l). The latter is a manifestation of the double ITCZ problem (Fig. 3j). Besides an overestimation of precipitation and clouds in the southern hemispheric deep tropics, the double ITCZ also results in too frequent subtropical high clouds. We further show the cross-sections for the MPI-ESM model individually (Fig. 3m-o), as it is used to compute the climate delta for the PGW simulation. The double ITCZ problem is more pronounced in the MPI-ESM model than in the CMIP6-EM and results in a bimodal annual mean precipitation distribution that is almost symmetric about the equator.

In ERA5, the cloud field at the ITCZ consists of (i) a concentration of low-level clouds, (ii) a secondary liquid cloud maximum at around 5 km (which appears to be related to an elevated inversion layer), and (iii) the deep-convective anvil clouds between 8-15 km altitude. In the subtropics, the free troposphere contains virtually no clouds below 10 km as a result of the stable and dry conditions in the downward branch of the HC. At the surface, low clouds are topping the MBL. The MBL is less shallow south of the equator than north of the equator. In the former case, the MBL is located further off the coastal upwelling regions of Africa, and thus experiences warmer sea surface temperature (SST) favoring the development of a deep MBL (e.g. Bretherton & Wyant, 1997). Beyond 25°S, clouds of extra-tropical origin penetrate into the subtropical atmosphere, in particular at high altitudes, where they contribute to the subtropical high-cloud fraction.

316 The annual mean and seasonal structure of ITCZ clouds in CTRL corresponds well
 317 with ERA5 (Fig. 3a-c,g-i). The main difference is that in the annual mean and during
 318 Feb-Apr, the extra-tropical clouds reach less far into the subtropics in CTRL. Overall,
 319 the differences are not fundamental and we conclude that CTRL simulates the cloud field
 320 along the HC consistent with ERA5. In contrast, the CMIP6-EM does not reproduce
 321 the vertical cloud structure at the ITCZ as seen in ERA5 and CTRL (Fig. 3d-f,j-l). In-
 322 stead, many of the analysed CMIP6 members simulate a too coherent cloud field through-
 323 out the tropical tropospheric column which also penetrates too high up into the trop-
 324 ical tropopause layer in some models. Although the focus of this study lies on marine
 325 clouds, the structure of the HC over land is shown in supplementary Fig. S6. While the
 326 vertical cloud structure in CTRL is comparable to ERA5, the high-cloud fraction and
 327 surface precipitation is significantly larger than in ERA5 and GPM IMERG. These quan-
 328 tities are both related to deep convection and thus indicate that deep convection at the
 329 continental ITCZ may be overestimated in CTRL, as will be shown later.

330 The first two columns of Fig. 4 show the large-scale overturning motion of the HC
 331 in terms of the meridional and vertical mass flux along the HC-CS domain. Air rises at
 332 the surface of the ITCZ and diverges above an altitude of 10 km towards the poles. The
 333 poleward (i.e., the elevated) branch of the HC converges with the northward branch of
 334 the Ferrel cell at 15°S in ERA5 (Fig. 4a) which sets the latitude of strongest subtrop-
 335 ical subsidence (Fig. 4b). The HC is closed by the trade winds at the surface that are
 336 largely confined to the MBL and converge at 5°N (Fig. 4a).

337 Compared to ERA5, the poleward branch of the HC in the southern hemisphere
 338 reaches further south in CTRL and the CMIP6-EM (Fig. 4a,e,i). Consequently, the sub-
 339 tropical subsidence extends further south in CTRL and the CMIP-EM than in ERA5
 340 (Fig. 4b,f,j). This dynamical difference between CTRL and ERA5 is consistent with the
 341 differences in the high-cloud fraction of extra-tropical origin at around 20°S between CTRL
 342 and ERA5 (Fig. 3a,g). A further difference between CTRL and ERA5 is related to the
 343 ITCZ outflow in the lower troposphere. ERA5 shows a pronounced shallow circulation
 344 between $2 \text{ km} < z < 6 \text{ km}$ (Fig. 4a) which is much weaker in CTRL (Fig. 4e). Thus, while
 345 the HC in ERA5 has a pronounced dual circulation structure (i.e. a deep circulation and
 346 a shallow circulation), the shallow circulation is almost absent in CTRL and the deep
 347 circulation is stronger (Fig. 4m). In line with that, the subtropical subsidence profile in
 348 ERA5 shows a pronounced maximum at 3 km (Fig. 4b), while it is more constant through-

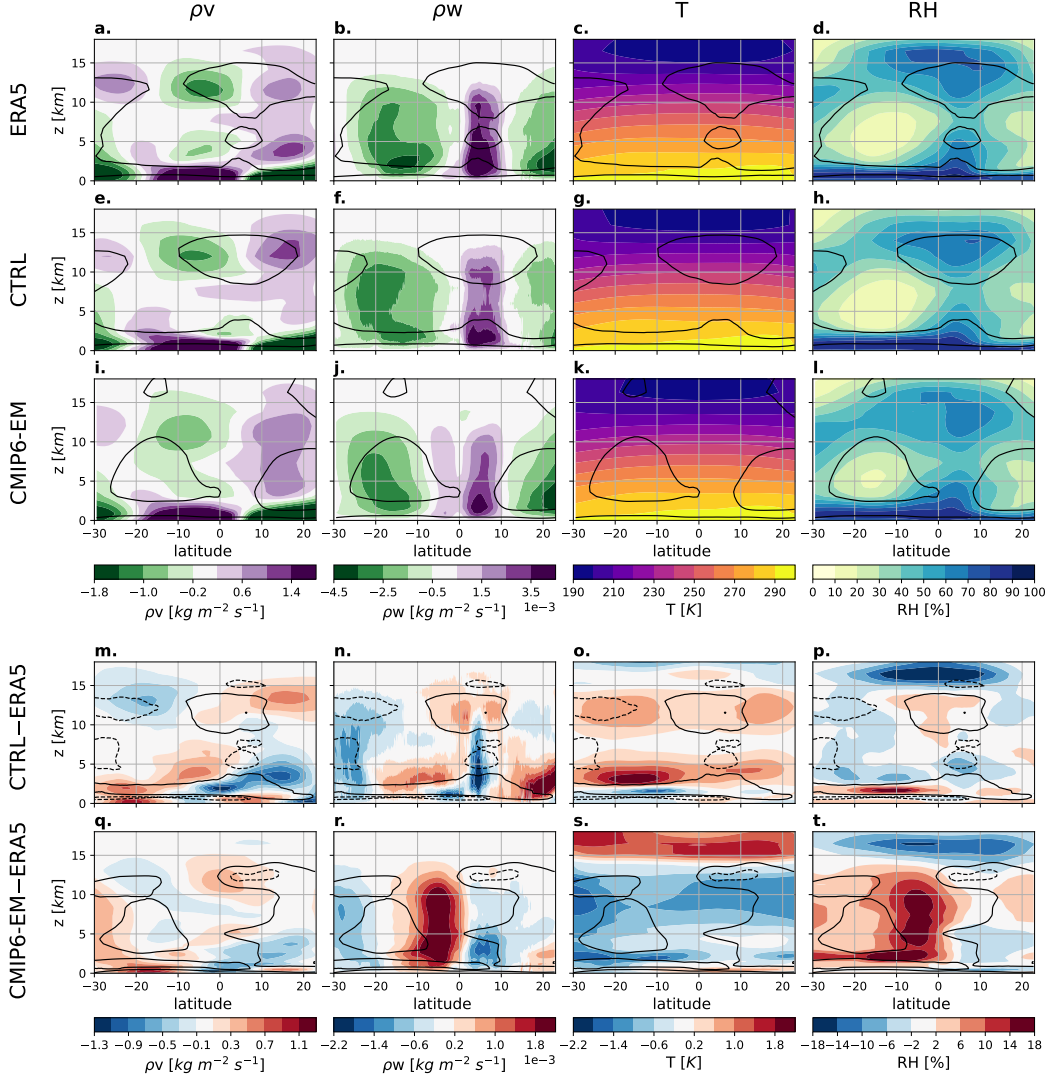


Figure 4. Annual mean altitude-latitude cross-sections of (first column) meridional mass flux [$\text{kg m}^{-2} \text{s}^{-1}$], (second column) vertical mass flux [$\text{kg m}^{-2} \text{s}^{-1}$], (third column) temperature [K], and (fourth column) relative humidity [%] averaged along the longitudes of the HC-CS domain. The panels show (a-d) ERA5 (2007-2010), (e-h) CTRL (2007-2010), (i-l) CMIP6-EM HIST (1985-2014), and the difference between (m-p) CTRL and ERA5 (2007-2010), and (q-t) CMIP6-EM HIST and ERA5 (1985-2014). The black contour lines indicate (a-l) the 5% cloud fraction level and (m-t) the 2% level of difference in the cloud fraction level where solid (dashed) lines represent a positive (negative) difference.

out the troposphere in CTRL (Fig. 4f). Differences in subsidence can result from differences in the radiative cooling rate or temperature stratification. The weaker subtropical subsidence at low levels in CTRL appears to be due to weaker radiative cooling rate compared to ERA5 (see supplementary Fig. S7). The meridional outflow of the ITCZ in the CMIP6-EM (Fig. 4i) is more evenly distributed over the free-tropospheric column compared to CTRL and ERA5, in line with the evenly distributed cloud fraction (Fig. 3j-l). Further, the imprint of the double ITCZ is well visible in the bias of the vertical wind field, showing an anomalous upward motion south of the equator compared to ERA5 (Fig. 4r).

The third and fourth columns of Fig. 4 show the thermodynamic structure of the HC along the HC-CS domain. Temperature in CTRL does not deviate from ERA5 by more than 1 K except in the subtropical lower troposphere (Fig. 4o). The differences in relative humidity between CTRL and ERA5 (Fig. 4p) are also small except for altitudes above 15 km where temperatures are very low and small differences in the amount of deep-convective outflow have a large effect on the relative humidity. Overall, the subtropical troposphere is slightly drier in CTRL than in ERA5, and (as for temperature) the differences are largest in the lower troposphere. The trade-wind inversion in CTRL is more elevated than in ERA5 which explains the lower temperature and enhanced humidity in CTRL in between (i.e. between 1-2 km). Above the inversion, the differences may be related to lower-tropospheric mixing which alters the moisture content of the free troposphere and thus modulates the clear-sky radiative cooling rate. The drier free troposphere in CTRL (Fig. 4p) may thus explain the weaker radiative cooling rate at these levels (Fig. S7), and consequently the warmer temperature (Fig. 4o) and weaker subsidence (Fig. 4n) in the subtropical lower troposphere in CTRL. The biases in temperature and relative humidity in the CMIP6-EM (Fig. 4s,t) are larger than in CTRL. This is expected since CTRL is driven by ERA5 at its boundaries while the CMIP6 simulations are global. Tropospheric temperature is lower in the CMIP6-EM than in ERA5 while stratospheric temperature is higher (Fig. 4s). Further, the deep tropics in the southern hemisphere are much moister than in ERA5, due to the double ITCZ (Fig. 4t).

3.1.2 Tropical Cloud Regimes

We continue with a more detailed evaluation of clouds and precipitation. Figure 5 shows the annual mean spatial pattern of the TOA albedo, surface precipitation, and TOA OLR. The low-cloud albedo is substantially overestimated in CTRL (Fig. 5c). Surface

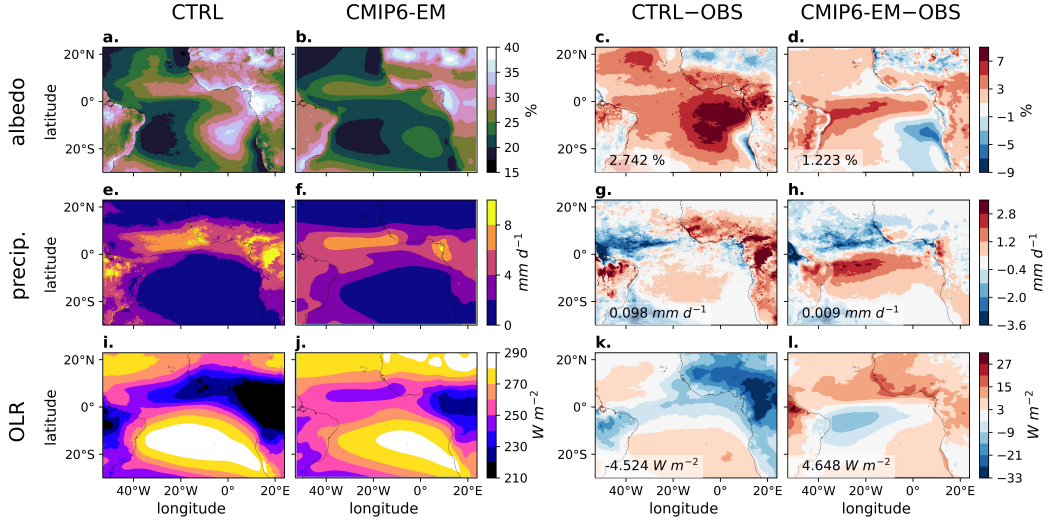


Figure 5. Evaluation of (a-d) TOA albedo [%], (e-h) surface precipitation [mm d^{-1}], and (i-l) TOA outgoing longwave radiation (OLR) [W m^{-2}]. The panels show (first column) CTRL (2007-2010), (second column) CMIP6-EM HIST (1985-2014), (third column) CTRL - OBS (2007-2010), and (fourth column) CMIP6-EM HIST (1985-2014) - OBS, where OBS is (c,d,k,l) the CM SAF record during (c,k) 2007-2010 and (d,l) 2004-2010, and (g,h) the GPM IMERG record during (g) 2007-2010 and (h) 2001-2014. The comparison between the CMIP6-EM and the OBS is thus based on the longest available observational period overlapping with HIST. The labels in the lower-left corners show domain average biases.

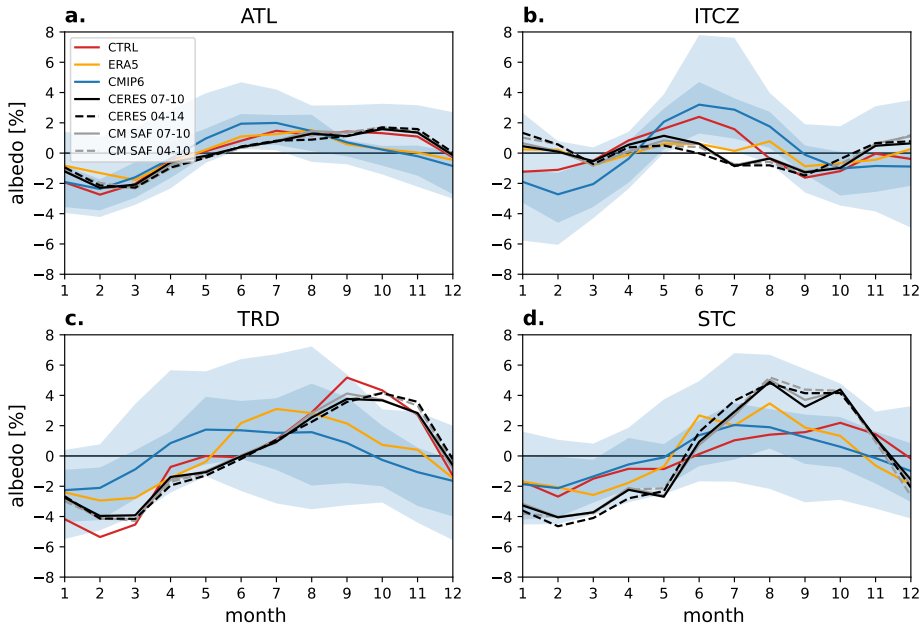


Figure 6. Evaluation of the mean annual cycle of TOA albedo shown for the four marine analysis domains (a) ATL, (b) ITCZ, (c) TRD and (d) STC. The annual cycle, expressed as the deviation from the annual mean, is shown for CTRL (2007-2010, red), ERA5 (2007-2010, yellow), CMIP6-EM HIST (1985-2014, blue), CERES EBAF (2007-2010, solid black), CERES EBAF (2004-2014, dashed black), CM SAF (2007-2010, solid gray), and CM SAF (2004-2010, dashed gray). The shading shows the CMIP6 ensemble spread between the 10th and 90th percentile (light blue) and the interquartile range (dark blue). Only ocean grid points are used in this figure.

381 precipitation in CTRL is overestimated over land in comparison to the GPM IMERG
 382 data set (Fig. 5g). The precipitation of the marine ITCZ is well represented to the East,
 383 but its westward extent is underestimated. OLR is far too low over land (Fig. 5k), in line
 384 with the precipitation bias. Over sea, the underestimation of OLR in the deep tropics
 385 is smaller, but subtropical OLR is overestimated. The CMIP6-EM bias patterns of these
 386 three variables (Fig. 5d,h,l) reveal the two well-known deficits of GCMs over low-latitude
 387 oceans: The double ITCZ problem and the underestimation of stratocumulus clouds. Also
 388 note that over land, the CMIP6-EM shows much smaller biases than CTRL.

389 We continue with the evaluation of the annual cycle of clouds on the four marine
 390 analysis domains ATL, ITCZ, TRD and STC. Figure 6 shows the mean annual cycle of
 391 TOA albedo in CERES EBAF, CM SAF, CTRL, ERA5, and the CMIP6 mean and en-

Table 1. Domain and time average values of TOA albedo [%], precipitation [mm d^{-1}] and OLR [W m^{-2}] on the four marine analysis domains ATL, ITCZ, TRD and STC shown for CTRL (2007-2010), ERA5 (2007-2010), CMIP6-EM HIST (1985-2014) and the satellite observations (CERES EBAF and CM SAF for albedo and OLR, and GPM IMERG for precipitation). As in Figs. 6-8, the satellite observations are listed during the CTRL period (2007-2010) and during the longest period overlapping with the HIST period (2004-2014 for CERES EBAF, 2004-2010 for CM SAF, and 2001-2014 for GPM IMERG).

albedo. [%]	ATL	ITCZ	TRD	STC
CTRL	24.5	24.5	23.8	27.7
ERA5	21.5	22.0	20.1	21.6
CMIP6-EM	22.2	23.1	20.6	22.2
CERES EBAF 07-10	21.1	21.4	18.8	24.4
CERES EBAF 04-14	21.2	21.3	18.8	24.7
CM SAF 07-10	20.9	20.9	18.8	24.5
CM SAF 04-10	21.0	21.0	18.9	24.9
precip. [mm d^{-1}]	ATL	ITCZ	TRD	STC
CTRL	2.10	4.15	0.95	0.37
ERA5	2.45	5.12	0.91	0.30
CMIP6-EM	2.46	4.58	1.72	0.52
GPM IMERG 07-10	2.44	5.01	0.57	0.20
GPM IMERG 01-14	2.33	4.78	0.49	0.19
OLR [W m^{-2}]	ATL	ITCZ	TRD	STC
CTRL	262.4	248.0	280.4	274.4
ERA5	269.5	259.4	285.0	279.3
CMIP6-EM	264.2	255.4	273.9	275.8
CERES EBAF 07-10	267.4	255.6	283.7	277.3
CERES EBAF 04-14	267.7	256.4	284.2	277.5
CM SAF 07-10	261.3	250.5	277.2	269.7
CM SAF 04-10	261.5	251.0	277.8	270.0

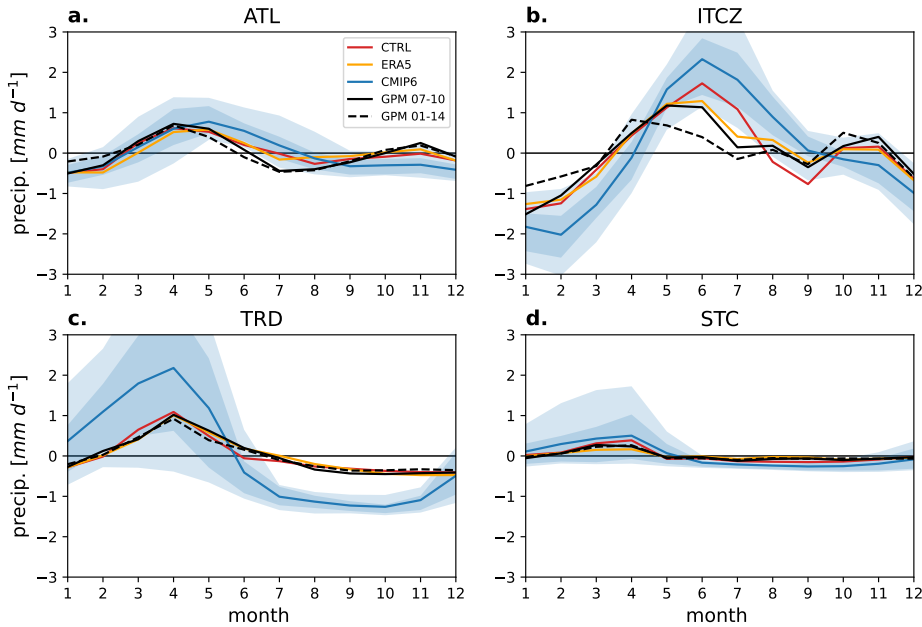


Figure 7. As Fig. 6 but showing surface precipitation. The black lines show GPM IMERG (2007-2010, solid) and GPM IMERG (2001-2014, dashed).

semble spread. The annual cycle is expressed as deviations from the annual mean. Table 1 lists the annual mean values for all data sets and analysis domains. Both observational records (CERES EBAF in black and CM SAF in grey) show very similar results for albedo, and are shown during the CTRL period (2007-2010, solid lines), but also during the longest available period overlapping with HIST (i.e. 2004-2014 and 2004-2010, dashed lines) to assess the effect of inter-annual variability. The annual cycle of the 4-year-period is very similar as in the extended period, indicating that the former is representative of the long-term conditions. Table 1 shows that the marine albedo in CTRL is overestimated by approximately 3.5%. However, the timings of annual maximum and minimum cloud cover as well as the amplitude of the annual cycle are much improved in CTRL compared to the CMIP6-EM on the ATL (Fig. 6a) and the TRD (Fig. 6c) domains, where CTRL even outperforms the ERA5 record. On the ITCZ (Fig. 6b) and the STC (Fig. 6d) domains, on the other hand, similar (though mitigated) deficiencies as in the CMIP6-EM are visible, i.e., an overestimation and underestimation of the ITCZ albedo during boreal summer and winter, respectively, as well as an underestimation of the annual cycle on the STC domain.

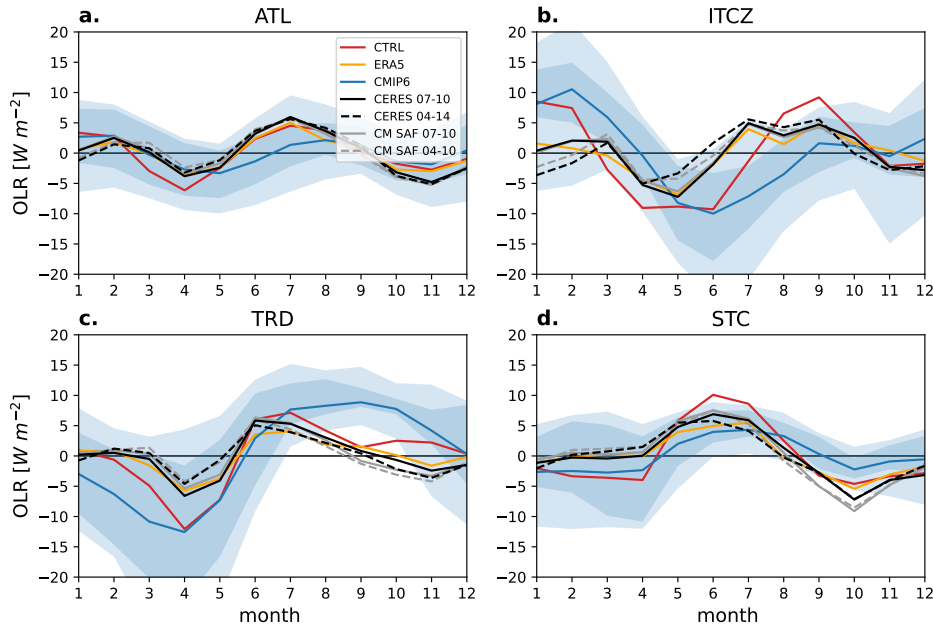


Figure 8. As Fig. 6 but showing TOA outgoing longwave radiation (OLR).

408 Figure 7 shows the annual cycle of surface precipitation over the marine analysis
 409 domains. The annual cycle is overall well represented in CTRL with the largest deviations
 410 found over the ITCZ domain (Fig. 7b), where the simulated timing of maximum
 411 precipitation lags one month behind the observed due to an overestimation of the bo-
 412 real summer precipitation (similar as for the albedo in Fig. 6). The relative difference
 413 in precipitation amount between the different domains is well simulated in CTRL, but
 414 with slightly more precipitation on the TRD and the STC domains compared to GPM IMERG
 415 (Table 1). In the CMIP6-EM, the precipitation amount over the TRD is overestimated
 416 more strongly due to the double ITCZ problem.

417 The annual cycle of OLR is shown in Fig. 8. Unlike for the albedo, there is a sur-
 418 prisingly large difference between CERES EBAF and CM SAF of about 6 W m^{-2} (Ta-
 419 ble 1). ERA5 is closer to CERES EBAF. The amplitude of the annual cycle of OLR in
 420 CTRL is overestimated on the three small analysis domains (ITCZ, TRD and STC; Fig. 8b-
 421 d). This appears to be mainly due to an overestimated high-cloud fraction originating
 422 at the ITCZ during the first half of the year and resulting in too much downwelling long-
 423 wave radiation. We further see a signal of too high tropospheric water vapor content (not
 424 shown) originating from the African ITCZ which contributes to the opacity of the at-

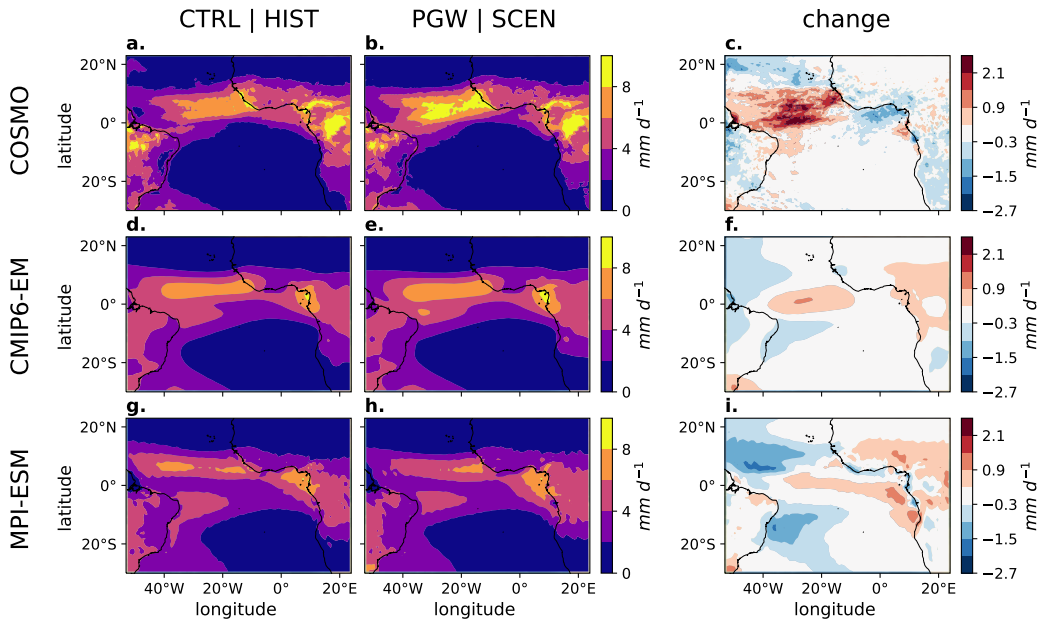


Figure 9. Annual mean climate-change signal of mean surface precipitation [mm d^{-1}]. The panels show (a-c) CTRL (2007-2010) and PGW (2007-2010), (d-f) the CMIP6-EM for HIST (1985-2014) and SCEN (2070-2099), and (g-i) the MPI-ESM model for HIST and SCEN. The columns show the simulated precipitation during (first column) CTRL and HIST, (second column) PGW and SCEN, and (third column) the change between CTRL and PGW, and between HIST and SCEN, respectively. CTRL and PGW are remapped to a 50 km grid.

mosphere over the Atlantic. Similar as for precipitation, the error of CTRL is largest over the ITCZ domain (Fig. 8b).

3.2 Application of PGW

We continue with the analysis of the climate change signal obtained from the PGW simulation (see Section 2.2). Figure 9 shows the annual mean spatial distribution of surface precipitation change between CTRL and PGW, and between HIST and SCEN. Marine ITCZ precipitation strongly increases in PGW, in some locations by up to 50% (Fig. 9c). Averaged over the ITCZ and ATL domains, precipitation increases by $7\% \text{K}^{-1}$ and $2\% \text{K}^{-1}$ respectively. The temperature change for this computation was evaluated at 1 km altitude which roughly corresponds to the cloud base (Fig. 3g). Consistent with the CMIP6-EM (Fig. 9f), the precipitation change in COSMO (Fig. 9c) is most pronounced in the center of the Atlantic, rather than along the West-African coastline (as, e.g., in the MPI-

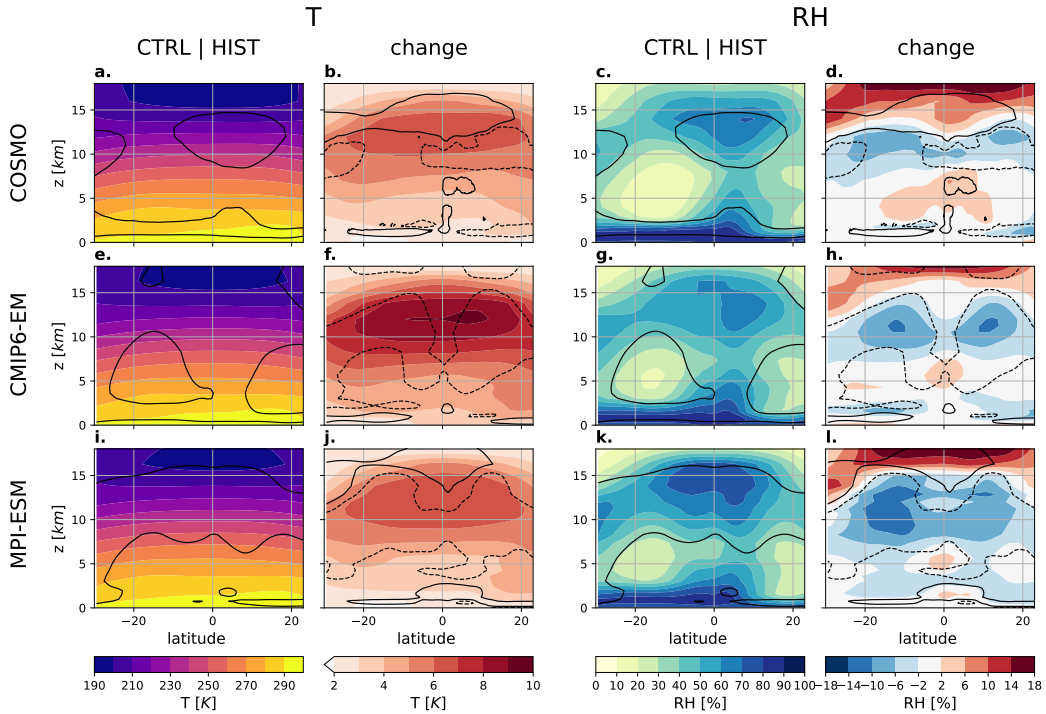


Figure 10. Annual mean altitude-latitudinal cross-sections of the climate-change signal of (left panels) temperature [K] and (right panels) relative humidity [%] averaged along the longitudes of the HC-CS domain. The panels show (a-d) CTRL and PGW (2007-2010), (e-h) CMIP6-EM HIST (1985-2014) and SCEN (2070-2099), and (i-l) MPI-ESM HIST and SCEN. The first and third columns show CTRL and HIST, while the second and fourth columns show the respective changes PGW-CTRL and SCEN-HIST. Panels (j,l) correspond to the climate delta from the MPI-ESM model used to derive the PGW simulation. The black contour lines indicate (first and third columns) the 5% cloud fraction level and (second and fourth columns) the level of 1% cloud fraction change where solid (dashed) lines represent a positive (negative) change.

437 ESM; Fig. 9i). Also consistent is the southward propagation of the precipitation max-
 438 imum, i.e., the most pronounced change is located to the South of the precipitation max-
 439 imum in CTRL/HIST (see also Fig. 11). However, unlike in the CMIP6-EM, there is no
 440 substantial precipitation reduction in the West Atlantic trades, and precipitation over
 441 land is reduced, instead of increased. Finally, while the precipitation changes in the CMIP6-
 442 EM and the MPI-ESM associated with the ITCZ are relatively symmetric about the equa-
 443 tor as a result of the double ITCZ, this is not the case in COSMO which does not show
 444 a double ITCZ.

Figure 10 shows the change in the thermodynamic structure of the HC. The temperature change PGW–CTRL (Fig. 10b) is similar to SCEN–HIST of the MPI-ESM (Fig. 10j) but slightly smaller overall. The similarity is expected since the latter is the climate delta used to derive the PGW boundary conditions. Tropospheric relative humidity decreases in the CMIP6 models (Fig. 10h,l) which is a reflection of the overall drying of the tropics, with the exception of a moistening deep-tropical lower troposphere (e.g. Lau & Kim, 2015). COSMO projects a qualitatively similar humidity change pattern (Fig. 10d) as the CMIP6 models, but with a weaker drying of the upper troposphere, a stronger moistening of the lower troposphere in the deep tropics, and – unlike in the CMIP6 models – this signal of increased humidity reaches the subtropics. Note that the relative humidity increase in the tropopause layer in all models appears to be associated with a comparably weak temperature increase due to enhanced longwave radiative cooling (Shine et al., 2003) and enhanced vertical moisture transport (Lau & Kim, 2015).

Figure 11 shows the simulated changes in the cloud field along the HC-CS domain. The signal PGW–CTRL (Fig. 11c) shows a rise of the anvil clouds at the ITCZ accompanied by a strong increase in the high-cloud fraction. In the CMIP6-EM (Fig. 11f), the rise of the high clouds is barely visible in the cloud field change, but will be visible in the meridional wind change (see Fig. 12f). In contrast to COSMO, both the CMIP6-EM (Fig. 11f) and the MPI-ESM (Fig. 11i) exhibit a deep-tropics squeeze, i.e. a reduction of the cloud fraction at the poleward margins of the annual mean ITCZ. Note that this reduction is visible at both instances of the double ITCZ (the real one north of the equator and the spurious one south of the equator). As a result of the deep-tropics squeeze, the ITCZ deep convection and precipitation in SCEN (Fig. 11e,h) is slightly more concentrated around the equator than in HIST (Fig. 11d,g). Finally, we note that the change PGW–CTRL (Fig. 11c) in trade wind clouds exhibits an opposite sign in the North and South Atlantic, unlike in SCEN–HIST (Fig. 11f,i) where shallow cloud cover decreases in both hemispheres.

The circulation changes along the HC-CS domain are shown in Fig. 12 in terms of the meridional and vertical mass fluxes. COSMO simulates an upward shift (maxima rise from approximately 12 km to 14 km) and a shallower upper-level meridional outflow (lower boundary rises more than upper boundary) of the ITCZ in PGW compared to CTRL (Fig. 12a-c). This change pattern qualitatively agrees with the CMIP6-EM (Fig. 12d-f) and the MPI-ESM (Fig. 12g-i), but the change in magnitude is slightly stronger com-

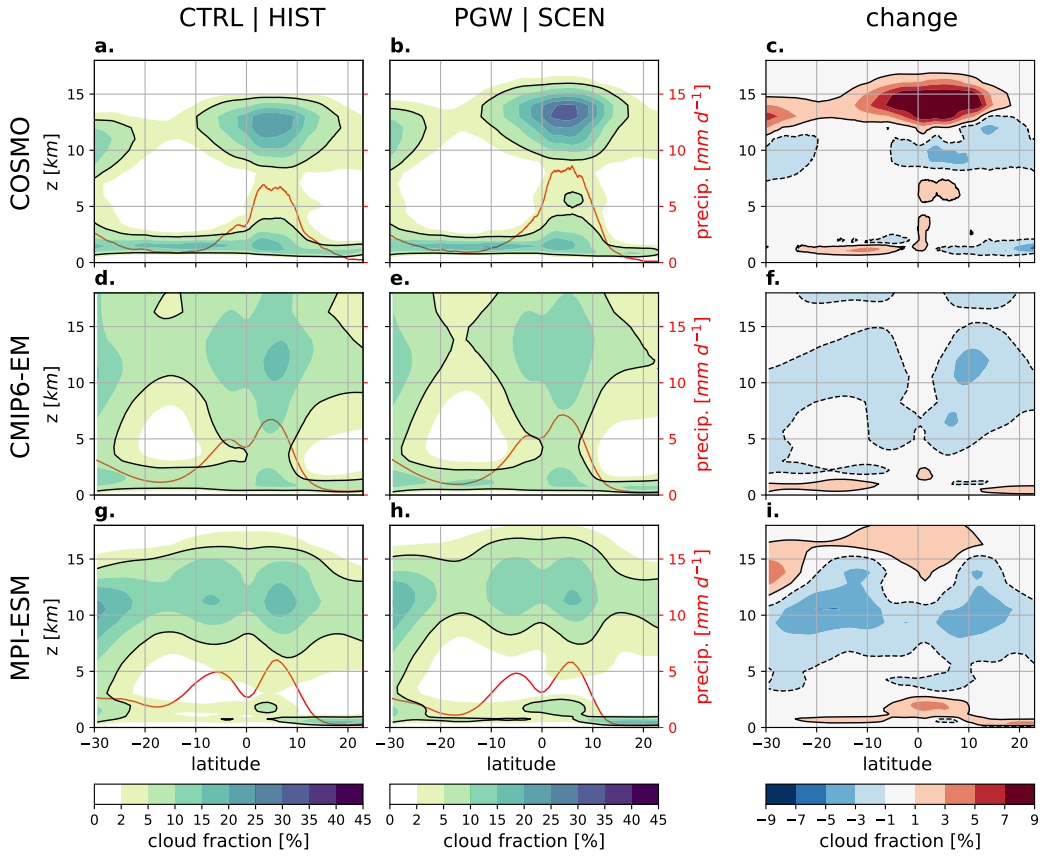


Figure 11. Annual mean altitude-latitude cross-sections of the cloud fraction [%] averaged along the longitudes of the HC-CS domain shown for (a-b) CTRL and PGW (2007-2010), (c) PGW-CTRL, (d) CMIP6-EM HIST (1985-2014), (e) CMIP6-EM SCEN (2070-2099), (f) CMIP6-EM SCEN-HIST, (g) MPI-ESM HIST, (h) MPI-ESM SCEN, and (i) MPI-ESM SCEN-HIST (i.e. corresponding to the climate delta used to derive the PGW simulation). (left and middle panels) The black contour lines high-light the 5% cloud fraction level. The red lines show surface precipitation [mm d^{-1}] represented on the scale of the right y-axis. (right panels) The black contour lines show the 1% level of cloud fraction change where solid (dashed) lines represent a positive (negative) change.

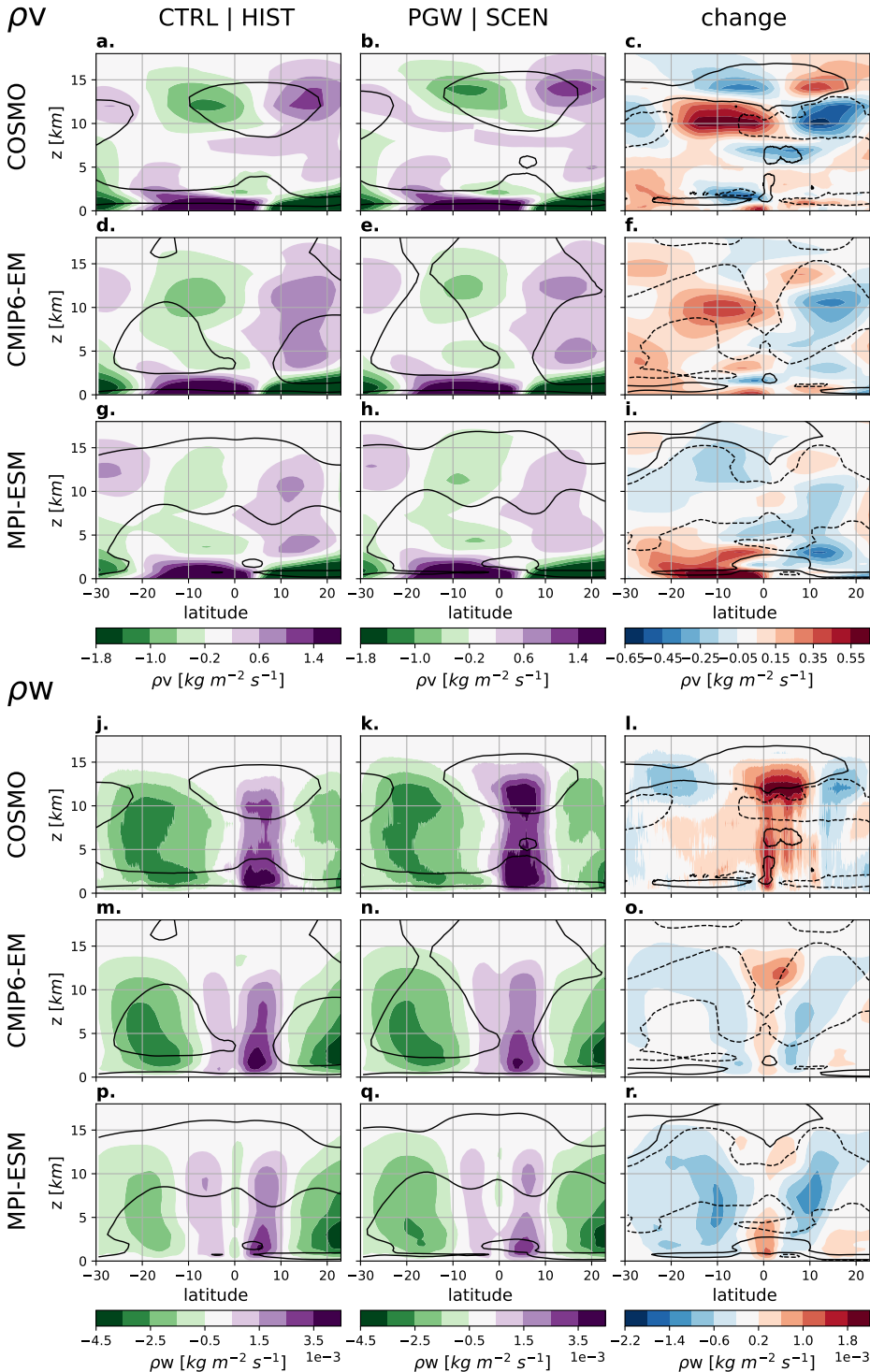


Figure 12. Annual mean altitude-latitudinal cross-sections of the climate change signal of (a-i) meridional mass flux ρ_v and (j-r) vertical mass flux ρ_w [$\text{kg m}^{-2} \text{s}^{-1}$] averaged along the longitudes of the HC-CS domain. The panels show (a-c,j-l) CTRL and PGW (2007-2010), (d-f,m-o) CMIP6-EM HIST (1985-2014) and SCEN (2070-2099), and (g-i,p-r) MPI-ESM HIST and SCEN. The first column shows CTRL and HIST, the second PGW and SCEN, and the third column shows the respective changes PGW-CTRL and SCEN-HIST. Panels (i,r) correspond to the climate delta from the MPI-ESM model used to derive the PGW simulation. The black contour lines indicate (first and second columns) the 5% cloud fraction level and (third column) the level of 1% cloud fraction change where solid (dashed) lines represent a positive (negative) change.

478 pared to the CMIP6-EM, and substantially stronger compared to the MPI-ESM. Along
 479 with the change in the meridional wind, the upward motion at the ITCZ in COSMO reaches
 480 higher levels and intensifies (Fig. 12j-l). The intensification occurs over the entire tro-
 481 pospheric column, but most pronounced above 10 km altitude. This response of the ITCZ
 482 to warming in COSMO shows remarkable differences to the CMIP6 models (Fig. 12m-
 483 r): First, the intensification of the ITCZ above 10 km is significantly stronger in COSMO
 484 than in the CMIP6 models (compare Figs. 12l and 12o,r), and – with a vertical exten-
 485 sion of about 2 km, i.e. from around 13 km to 15 km altitude (Fig. 12j,k) – the deepen-
 486 ing of the ITCZ is larger compared to the CMIP6-EM (about 1 km, from around 12 km
 487 to 13 km, Fig. 12m,n). Second, the change of the ITCZ below 10 km represents a response
 488 that differs from the deep-tropics squeeze. While the CMIP6 models simulate a weak-
 489 ening of the upward motion at the margins of the deep-tropics and only a weak inten-
 490 sification at the equator (i.e. the deep-tropics squeeze; Fig. 12o,r), COSMO simulates
 491 an extension of the ITCZ towards south and an intensification over the entire meridional
 492 extent of the CTRL ITCZ (Fig. 12j,l).

493 With respect to subtropical subsidence, the response of COSMO also differs from
 494 the CMIP6 models. First, the strengthening of subsidence is mostly confined to the edge
 495 of the cloud anvils above 10 km and extends less prominently through the tropospheric
 496 column than in the CMIP6-EM and the MPI-ESM. In the northern hemisphere, the sub-
 497 sidence intensification below 10 km is still comparable to the CMIP6 models (even though
 498 confined to the subtropics), but in the southern hemisphere, there is an overall weaken-
 499 ing of annual mean subsidence in COSMO, as opposed to the strengthening in the CMIP6
 500 models. Finally, the intensification of subtropical subsidence above 10 km is substantially
 501 larger in COSMO than in the CMIP6-EM, consistent with the more pronounced deep-
 502 ening and upper-level intensification of the ITCZ deep convection.

503 4 Discussion

504 4.1 Evaluation of CTRL

505 In Section 3, we discussed the realism of the ERA5-driven CTRL simulation in com-
 506 parison to the CMIP6-EM and found significant differences. As the two underlying sim-
 507 ulation strategies differ strongly, it is not feasible to disentangle effects due to compu-
 508 tational resolution (3 km versus 50-200 km) and simulation setup (ERA5 driven atmo-

509 spheric simulations versus free-running coupled simulations). The main purpose of the
 510 following discussion is thus to summarize the differences between the CTRL simulation
 511 and the CMIP6 ensemble, and to determine whether the ERA5-driven simulations are
 512 credible enough to serve as the basis of climate-change simulations using the PGW ap-
 513 proach.

514 The improved representation of the annual cycle of the albedo, in particular on the
 515 TRD analysis domain (representative of shallow cumulus clouds), as well as the accu-
 516 rate vertical structure and meridional position of the ITCZ (i.e. no double ITCZ) are per-
 517 haps the most promising improvements compared to the CMIP6-EM. The prescribed SST
 518 obtained from ERA5 likely has a beneficial impact on the properties of the MBL and
 519 the position of the ITCZ in CTRL. For instance, the double ITCZ problem of the CMIP6-
 520 EM is thought to be related to air-sea interaction, among other factors (Lin, 2007; Li
 521 & Xie, 2014). It would therefore be interesting to test if for instance a coupled model
 522 setup at kilometer-resolution or a GCM-driven kilometer-resolution simulation were to
 523 suffer from the double ITCZ problem. Under the assumption that the improved repre-
 524 sentation of the ITCZ in our limited-area CTRL simulation is due to the forcing from
 525 ERA5, our application demonstrates one benefit of the PGW approach compared to con-
 526 ventional downscaling, i.e. that GCM circulation biases are not propagated to the limited-
 527 area simulation. We argue that this realistic representation of the ITCZ location is a good
 528 starting point to study its climate change signal.

529 Concerning the simulation of low clouds, the representation of the annual cycle of
 530 the albedo in CTRL is better on the TRD domain than on the STC domain. This dis-
 531 crepancy may relate to the type of clouds most prevalent on the two domains. The TRD
 532 domain is predominantly covered by trade-wind cumulus clouds while stratocumulus clouds
 533 are more frequent on the STC domain (Warren et al., 1988). The difficulty to represent
 534 the annual cycle of stratocumulus clouds in a kilometer-resolution model with 60 ver-
 535 tical levels is not unexpected since a firm representation of the stratocumulus-topped MBL
 536 with its very shallow inversion cloud layer is challenging even in LES (e.g. Stevens et al.,
 537 2005). Nevertheless, the fact that the COSMO simulations yield stratocumulus decks
 538 already at kilometer-resolution, notably without any shallow convection scheme, is very
 539 promising. In the trade-wind cumulus regime clouds often aggregate into clusters that
 540 frequently exceed the kilometer-scale (e.g. Bony et al., 2020). The CTRL simulation in-
 541 deed produces such clusters (see Fig. 2) suggesting that some of the dominant mesoscale

patterns of MBL circulations and clouds in the Trades are at least partially resolved. Similar results have been found in previous studies using kilometer-resolution models (Klocke et al., 2017; Heim et al., 2021; Caldwell et al., 2021). It is interesting to note that the annual cycle of albedo in CTRL on the TRD domain is actually better simulated than in ERA5. This result suggests that the improved representation of these clouds is not primarily a result of the prescribed SST, but portrays the added value of explicit convection and fine model resolution.

On the other hand, we find a mean bias in the low-cloud albedo in the CTRL simulation compared to satellite observations (Fig. 5). This bias was found to be caused by an overestimation of cloud water (i.e., cloud opacity) rather than cloud fraction (Heim et al., 2021). As shown by Liu et al. (2022), this bias of the COSMO model at kilometer-resolution can be reduced through systematic model calibration. The model version used here is still based on a set of empirical parameters that were calibrated for applications over continental regions of the mid-latitudes (Bellprat et al., 2016). We also find a bias in quantities related to deep convection at the continental ITCZ over Africa (Fig. 5). Compared to the well calibrated COSMO simulations in the mid-latitudes (e.g. Leutwyler et al., 2017; Vergara-Temprado et al., 2020; Ban et al., 2021; Zeman et al., 2021), the bias in precipitation and OLR is still quite substantial. The set of empirical parameters used in this study differs from other COSMO setups that have been used over Africa (Bucchignani et al., 2016; Sørland et al., 2021). A calibration effort similar as it was done for the tropical Atlantic in Liu et al. (2022), but for continental Africa would likely result in a simulation setup with less biased deep convection overall. Note, it is possible that the poor representation of the continental ITCZ could affect the representation of the marine ITCZ via the lower-tropospheric mean easterly flow or via gravity waves (e.g. Leutwyler & Hohenegger, 2021).

4.2 Climate Change Signal PGW–CTRL

The changes SCEN–HIST in wind and humidity at the Atlantic HC compare qualitatively well to the global CMIP5 models (Lau & Kim, 2015). This agreement indicates that, despite the local computational domain employed, the obtained results may be indicative of the global patterns. Concerning the change signal in COSMO (PGW–CTRL), the tropospheric warming profile closely follows the climate delta (SCEN–HIST) of the MPI-ESM simulation (Fig. 10). This similarity is expected since the temperature change

574 is a large-scale signal that enters the model at the lateral boundaries (see Sec. 2.2). The
 575 change signal PGW–CTRL for humidity shows a qualitatively similar change pattern
 576 as the CMIP6-EM and the MPI-ESM, however, with an overall weaker drying of the trop-
 577 ical atmosphere (Fig. 10). The distribution of humidity is tied to the representation of
 578 deep convection and how it changes between CTRL and PGW (or HIST and SCEN).
 579 Since domain-average convection at the ITCZ intensifies in COSMO but weakens in the
 580 MPI-ESM model, some differences in the humidity change are expected.

581 The circulation changes, on the other hand, differ quite substantially between COSMO
 582 and the CMIP6 models. The intensification of deep convection at the ITCZ is remark-
 583 ably strong and accompanied by a widening of the ITCZ in the presented kilometer-resolution
 584 simulation. This result is novel, since GCM projections show an anti-correlation between
 585 strengthening and widening of the ITCZ between models (Byrne et al., 2018). Also, the
 586 rise of the anvil clouds is more pronounced than in the CMIP6 models, and the increase
 587 in the anvil cloud fraction is even contrary to the expectation of the stability iris hypoth-
 588 esis (Bony et al., 2016). In this respect, our simulation qualitatively differs from high-
 589 resolution simulations of radiative-convective equilibrium in aqua-planet configurations,
 590 whereof a majority shows a reduction in the high-cloud fraction with warming (Wing
 591 et al., 2020). Yet, the increase in tropical high clouds shows similarities to the response
 592 Satoh et al. (2012) found in their global kilometer-resolution short-term climate simu-
 593 lation. For this simulation, Tsushima et al. (2014) determined that the change in high
 594 ice clouds is sensitive to the formulation of subgrid turbulent mixing. The work of Tsushima
 595 et al. (2014); Ohno and Satoh (2018); Ohno et al. (2019, 2021) demonstrates that even
 596 at kilometer-resolution the response of tropical deep convection to warming may be sub-
 597 ject to extensive inter-model variability, and that the here presented results require cor-
 598 roboration from kilometer-resolution climate simulations employing other model codes,
 599 microphysics schemes, and downscaling approaches.

600 An often discussed hypothesis on the change in the dynamics of the HC is the promi-
 601 nent deep-tropics squeeze, i.e. the narrowing of the annual mean ITCZ, detectable in GCMs
 602 (e.g. Lau & Kim, 2015; Byrne & Schneider, 2016). In our CMIP6 ensemble, the squeeze
 603 is clearly evident in the form of a strengthening and narrowing of the deep-tropical con-
 604 vention and a corresponding reduction of cloud fraction at the edges of the ITCZ (Fig. 11
 605 and Fig. 12). However, this narrowing of the annual mean ITCZ seems to be enhanced
 606 by the fact that the CMIP6-EM projects a similar but mirrored change signal at both

branches of the ITCZ (i.e. the one north of the equator, and the spurious one south of the equator – the double ITCZ). This perception is supported by the fact that the narrowing of the ITCZ in GCMs is associated mainly with a northward shift of the southern edge (Byrne & Schneider, 2016). The deep-tropics squeeze can not be visually detected in the kilometer-resolution simulation which does not produce a double ITCZ in CTRL. So, the question arises whether the narrowing of the deep tropics in the CMIP6-EM would be equally pronounced if it did not exhibit the double ITCZ in HIST. The circulation changes projected by COSMO differ more prominently from CMIP6-EM at the southern edge of the ITCZ, suggesting that the double ITCZ may indeed contribute to the differences in the projected change. The double ITCZ was found to relate to the strength of the low-cloud feedback in GCMs (Tian, 2015) which was argued to be driven by differences in the lower-tropospheric stability depending on the strength of the double ITCZ (Webb & Lock, 2020). Whether and how the double ITCZ responds to warming and how this relates to radiative feedbacks is thus of high relevance for climate projections and requires further research.

There are some limitations of the model setup presented in this study. The COSMO model was originally designed as a weather prediction model, and aerosols and ozone are represented in a simplified manner compared to comprehensive climate models. Further, the one-moment microphysics scheme assumes a constant cloud-droplet number concentration. Changes in aerosol concentrations therefore do not directly alter the properties of the simulated clouds. Keeping ozone and aerosol concentrations constant between CTRL and PGW is thus a pragmatic choice for the given model configuration. Still, accounting for such effects might alter the simulated response to warming. For instance, the MPI-ESM shows an increase and slight upward shift of the ozone maximum between HIST and SCEN. Another simplification of the modelling setup in this study is the use of a limited-area model and the PGW approach. Given that the same weather enters the model domain at the boundaries in CTRL and PGW, large-scale circulation changes from the GCM may be restrained by the persistence of the weather phenomena at the lateral boundaries. Specifically, at the boundary between the subtropics and the mid-latitudes, it is unclear how the extension of the HC towards South with warming (e.g. Lau & Kim, 2015) is restrained by the fact that the mid-latitude frontal systems enter the PGW simulation at the same latitudes as in CTRL.

639 An interesting extension of this study would be to repeat the analysis using PGW
 640 simulations derived with climate deltas of different GCMs to test the sensitivity of the
 641 change signal PGW–CTRL to the climate delta. The role of SST warming patterns ap-
 642 pears to be of particular interest here. Given the importance of the SST pattern on changes
 643 of the ITCZ (Huang et al., 2013), it would not be surprising to find differences in the
 644 change PGW–CTRL in terms of structure and location of the ITCZ for different climate
 645 deltas.

646 5 Conclusion

647 In this study, we conducted what is, to our best knowledge, the first application
 648 of the pseudo-global warming (PGW) approach on a marine tropical domain that con-
 649 tains the entire Hadley circulation. We performed two 4-year-long simulations at 3.3 km
 650 horizontal resolution with the limited-area model COSMO over the tropical Atlantic. The
 651 analysis includes an evaluation of the structure of the Hadley circulation and tropical
 652 clouds under current climate conditions (CTRL), and a comparison of the obtained cli-
 653 mate change signal (PGW–CTRL) to that of a CMIP6 model ensemble (SCEN–HIST).
 654 The radiative feedback between CTRL and PGW will be analysed in a follow-up study.
 655 The main analysis findings include:

- 656 1. An improved representation of the vertical structure and seasonal cycle (in terms
 657 of the meridional location) of the Atlantic ITCZ compared to the CMIP6 ensem-
 658 ble. In particular, our limited area simulation with explicit convection does not
 659 suffer from the double ITCZ problem.
- 660 2. An improved representation of the annual cycle of the TOA albedo compared to
 661 the CMIP6 ensemble, in particular in the trade-wind cumulus region where CTRL
 662 even outperforms the ERA5 reanalysis. This suggests that kilometer-resolution
 663 simulations are a suitable tool to study cloud feedbacks in the trade-wind region.
 664 Despite disabling the models shallow convection scheme, stratocumulus clouds are
 665 evident, albeit somewhat too frequent, and with an underestimated amplitude of
 666 the annual cycle.
- 667 3. The dynamics of the ITCZ respond to warming in a different way in our kilometer-
 668 resolution simulation compared to the analysed GCMs. While the CMIP6 ensem-
 669 ble shows a narrowing and central intensification of the ITCZ, i.e. a prominent

670 deep-tropics squeeze, the kilometer-resolution simulation shows an overall inten-
 671 sification of the ITCZ, most pronounced at high altitudes, and a slight extension
 672 towards south.

673 Overall, our results demonstrate the merit of high-resolution climate simulations in a real-
 674 world configuration to compare against GCM projections. kilometer-resolution models
 675 enable an unprecedented view on tropical clouds and circulations from the large-scale
 676 tropical overturning circulation down to small-scale convective MBL circulations and clouds.
 677 Even though global kilometer-resolution climate simulations are not yet feasible, our study
 678 demonstrates that downscaling strategies like the PGW approach allow to gain insights
 679 from these models already today. We presented one such simulation that, compared to
 680 GCMs, produces a remarkably different climate-change response for the HC and in par-
 681 ticular for the ITCZ. The realism of this response is difficult to assess as long as such
 682 simulations remain a rarity. We will analyse in more detail the cause of the response in
 683 upcoming work.

684 6 Data Availability

685 The CERES EBAF TOA radiation data are available at <https://ceres-tool.larc.nasa.gov/ord-tool/jsp/EBAFTOA41Selection.jsp> via DOI:10.5067/TERRA-AQUA/CERES/
 686 EBAF-TOA_L3B004.1.
 687 The CM SAF TOA radiation data are available at <https://wui.cmsaf.eu/safira/action/viewProduktList?dId=3> via DOI:10.5676/EUM_SAF_CM/TOA_GERB/V002.
 688 The GPM IMERG precipitation data are available at <https://disc.gsfc.nasa.gov>
 689 via DOI:10.5067/GPM/IMERGDF/DAY/06.
 690 The ERA5 reanalysis data are available at the Copernicus Climate Change Service (C3S)
 691 Climate Data Store via DOI:10.24381/cds.bd0915c6.
 692 The CMIP6 data are available at the <https://esgf-node.llnl.gov/projects/cmip6/>.
 693 The software to prepare PGW simulations can be obtained from <https://github.com/Potopoles/pgw-python> via DOI:10.5281/zenodo.6759029.
 694 The weather and climate model COSMO is free of charge for research applications (for
 695 more details see: <http://www.cosmo-model.org>).

699 **Acknowledgments**

700 This work was funded by the Swiss National Science Foundation (SNSF) project “Ex-
 701 ploiting km-resolution climate models in the tropics to constrain climate change uncer-
 702 tainties” (trCLIM).

703 We acknowledge PRACE for awarding us access to Piz Daint at Swiss National Super-
 704 computing Center (CSCS, Switzerland). Furthermore, we acknowledge the COSMO, CLM
 705 and C2SM communities for developing and maintaining COSMO in climate mode, and
 706 the Federal Office for Meteorology and Climatology MeteoSwiss, CSCS, and ETH Zürich
 707 for their contributions to the development of the GPU-accelerated version of COSMO.
 708 We acknowledge the World Climate Research Programme, which, through its Working
 709 Group on Coupled Modelling, coordinated and promoted CMIP6. We thank the climate
 710 modeling groups for producing and making available their model output, the Earth Sys-
 711 tem Grid Federation (ESGF) for archiving the data and providing access, and the mul-
 712 tiple funding agencies who support CMIP6 and ESGF.

713 **References**

- 714 Adachi, S. A., & Tomita, H. (2020). Methodology of the Constraint Condition in
 715 Dynamical Downscaling for Regional Climate Evaluation: A Review. *Journal*
 716 *of Geophysical Research: Atmospheres*, 125(11). doi: 10.1029/2019JD032166
- 717 Baldauf, M., Seifert, A., Förstner, J., Majewski, D., Raschendorfer, M., & Rein-
 718 hardt, T. (2011, 12). Operational Convective-Scale Numerical Weather Predic-
 719 tion with the COSMO Model: Description and Sensitivities. *Monthly Weather*
 720 *Review*, 139(12), 3887–3905. Retrieved from <http://journals.ametsoc.org/>
 721 doi/abs/10.1175/MWR-D-10-05013.1 doi: 10.1175/MWR-D-10-05013.1
- 722 Ban, N., Caillaud, C., Coppola, E., Pichelli, E., Sobolowski, S., Adinolfi, M., ...
 723 Zander, M. J. (2021, 7). The first multi-model ensemble of regional climate
 724 simulations at kilometer-scale resolution, part I: evaluation of precipitation.
 725 *Climate Dynamics*, 57(1-2), 275–302. Retrieved from <https://doi.org/10.1007/s00382-021-05708-w> doi: 10.1007/s00382-021-05708-w
- 726 Bellprat, O., Kotlarski, S., Lüthi, D., De Elía, R., Frigon, A., Laprise, R., & Schär,
 727 C. (2016). Objective calibration of regional climate models: Application
 728 over Europe and North America. *Journal of Climate*, 29(2), 819–838. doi:

- 731 10.1175/JCLI-D-15-0302.1
- 732 Bellucci, A., Gualdi, S., & Navarra, A. (2010, 3). The double-ITCZ syndrome in
733 coupled general circulation models: The role of large-scale vertical circulation
734 regimes. *Journal of Climate*, 23(5), 1127–1145. doi: 10.1175/2009JCLI3002.1
- 735 Belušić, A., Prtenjak, M. T., Güttsler, I., Ban, N., Leutwyler, D., & Schär, C. (2018,
736 6). Near-surface wind variability over the broader Adriatic region: insights
737 from an ensemble of regional climate models. *Climate Dynamics*, 50(11–
738 12), 4455–4480. Retrieved from <http://dx.doi.org/10.1007/s00382-017-3885-5> doi:
739 10.1007/s00382-017-3885-5
- 740
- 741 Blossey, P. N., Bretherton, C. S., Zhang, M., Cheng, A., Endo, S., Heus, T., ... Xu,
742 K. (2013, 6). Marine low cloud sensitivity to an idealized climate change: The
743 CGILS LES intercomparison. *Journal of Advances in Modeling Earth Systems*,
744 5(2), 234–258. Retrieved from <https://onlinelibrary.wiley.com/doi/10.1002/jame.20025> doi: 10.1002/jame.20025
- 745
- 746 Bony, S., & Dufresne, J.-L. (2005). Marine boundary layer clouds at the heart of
747 tropical cloud feedback uncertainties in climate models. *Geophysical Research
748 Letters*, 32(20), L20806. Retrieved from <http://doi.wiley.com/10.1029/2005GL023851> doi: 10.1029/2005GL023851
- 749
- 750 Bony, S., Schulz, H., Vial, J., & Stevens, B. (2020, 4). Sugar, Gravel, Fish,
751 and Flowers: Dependence of Mesoscale Patterns of Trade-Wind Clouds
752 on Environmental Conditions. *Geophysical Research Letters*, 47(7). doi:
753 10.1029/2019GL085988
- 754
- 755 Bony, S., Stevens, B., Coppin, D., Becker, T., Reed, K. A., Voigt, A., & Medeiros,
756 B. (2016). Thermodynamic control of anvil cloud amount. *Proceedings of
757 the National Academy of Sciences of the United States of America*, 113(32),
8927–8932. doi: 10.1073/pnas.1601472113
- 758
- 759 Bott, A. (1989, 5). A Positive Definite Advection Scheme Obtained by Non-
760 linear Renormalization of the Advective Fluxes. *Monthly Weather Re-
761 view*, 117(5), 1006–1016. Retrieved from [https://doi.org/10.1175/1520-0493\(1989\)117%3C1006:APDASO%3E2.0.CO;2](https://doi.org/10.1175/1520-0493(1989)117%3C1006:APDASO%3E2.0.CO;2) doi:
762 10.1175/1520-0493(1989)117%3C1006:APDASO%3E2.0.CO;2
- 763 Bretherton, C. S. (2015, 11). Insights into low-latitude cloud feedbacks from high-

- resolution models. *Philosophical Transactions of the Royal Society A: Mathematical, Physical and Engineering Sciences*, 373(2054), 20140415. Retrieved from <https://royalsocietypublishing.org/doi/10.1098/rsta.2014.0415> doi: 10.1098/rsta.2014.0415
- Bretherton, C. S., & Wyant, M. C. (1997, 1). Moisture Transport, Lower-Tropospheric Stability, and Decoupling of Cloud-Topped Boundary Layers. *Journal of the Atmospheric Sciences*, 54(1), 148–167. Retrieved from [https://doi.org/10.1175/1520-0469\(1997\)054%3C0168:NSAACM%3E2.0.CO;2](https://doi.org/10.1175/1520-0469(1997)054%3C0168:NSAACM%3E2.0.CO;2) doi: 10.1175/1520-0469(1997)054(0148:MTLTSA)2.0.CO;2
- Brogli, R., Heim, C., Sørland, S. L., & Schär, C. (2022). The pseudo-global-warming (PGW) approach: Methodology, software package PGW4ERA5 v1.1, validation and sensitivity analyses. *Geoscientific Model Development, in review*. doi: 10.5194/gmd-2022-167
- Brogli, R., Kröner, N., Sørland, S. L., Lüthi, D., & Schär, C. (2019, 1). The Role of Hadley Circulation and Lapse-Rate Changes for the Future European Summer Climate. *Journal of Climate*, 32(2), 385–404. Retrieved from <http://journals.ametsoc.org/doi/10.1175/JCLI-D-18-0431.1> doi: 10.1175/JCLI-D-18-0431.1
- Bucchignani, E., Cattaneo, L., Panitz, H. J., & Mercogliano, P. (2016, 2). Sensitivity analysis with the regional climate model COSMO-CLM over the CORDEX-MENA domain. *Meteorology and Atmospheric Physics*, 128(1), 73–95. doi: 10.1007/s00703-015-0403-3
- Byrne, M. P., Pendergrass, A. G., Rapp, A. D., & Wodzicki, K. R. (2018, 12). *Response of the Intertropical Convergence Zone to Climate Change: Location, Width, and Strength* (Vol. 4) (No. 4). Springer. doi: 10.1007/s40641-018-0110-5
- Byrne, M. P., & Schneider, T. (2016, 11). Narrowing of the ITCZ in a warming climate: Physical mechanisms. *Geophysical Research Letters*, 43(21), 350–11. Retrieved from <https://onlinelibrary.wiley.com/doi/10.1002/2016GL070396> doi: 10.1002/2016GL070396
- Caldwell, P. M., Terai, C. R., Hillman, B., Keen, N. D., Bogenschutz, P., Lin, W.,

- 797 ... Zender, C. S. (2021, 11). Convection-Permitting Simulations With the
798 E3SM Global Atmosphere Model. *Journal of Advances in Modeling Earth*
799 *Systems*, 13(11). doi: 10.1029/2021MS002544
- 800 Chen, J., Wang, Z., Tam, C.-Y., Lau, N.-C., Lau, D.-S. D., & Mok, H.-Y. (2020, 12).
801 Impacts of climate change on tropical cyclones and induced storm surges in
802 the Pearl River Delta region using pseudo-global-warming method. *Scientific*
803 *Reports*, 10(1), 1965. doi: 10.1038/s41598-020-58824-8
- 804 Clerbaux, N., Nevens, S., & Decoster, I. (2013). CM SAF TOA Radiation "GERB"
805 dataset - Edition 1 - Monthly Means / Daily Means / Monthly mean diurnal
806 cycle, Satellite Application Facility on Climate Monitoring.
- 807 Copernicus Climate Change Service (C3S). (2017). ERA5: Fifth genera-
808 tion of ECMWF atmospheric reanalyses of the global climate. *Coperni-*
809 *cus Climate Change Service Climate Data Store (CDS)*. Retrieved from
810 <https://cds.climate.copernicus.eu/cdsapp#!/home>
- 811 Eyring, V., Bony, S., Meehl, G. A., Senior, C. A., Stevens, B., Stouffer, R. J.,
812 & Taylor, K. E. (2016, 5). Overview of the Coupled Model Intercom-
813 parison Project Phase 6 (CMIP6) experimental design and organiza-
814 tion. *Geoscientific Model Development*, 9(5), 1937–1958. Retrieved
815 from <https://gmd.copernicus.org/articles/9/1937/2016/> doi:
816 10.5194/gmd-9-1937-2016
- 817 Fiedler, S., Crueger, T., D'Agostino, R., Peters, K., Becker, T., Leutwyler, D.,
818 ... Stevens, B. (2020, 9). Simulated Tropical Precipitation Assessed
819 across Three Major Phases of the Coupled Model Intercomparison Project
820 (CMIP). *Monthly Weather Review*, 148(9), 3653–3680. Retrieved from
821 <http://journals.ametsoc.org/doi/10.1175/MWR-D-19-0404.1> doi:
822 10.1175/MWR-D-19-0404.1
- 823 Forster, P., Storelvmo, T., Armour, K., Collins, W., Dufresne, J.-l., Frame, D.,
824 ... Zhang, H. (2021). *The Earth's Energy Budget, Climate Feedbacks, and*
825 *Climate Sensitivity. In Climate Change 2021: The Physical Science Basis.*
826 *Contribution of Working Group I to the Sixth Assessment Report of the In-*
827 *tergovernmental Panel on Climate Change [Masson-Delmotte, V., P. Zhai,*
828 *A. Pirani, S.L. Connors, C. Péan, S. Berger, N. Caud, Y. Chen, L. Gold-*
829 *farb, M.I. Gomis, M. Huang, K. Leitzell, E. Lonnoy, J.B.R. Matthews, T.K.*

- 830 *Maycock, T. Waterfield, O. Yelekçi, R. Yu, and B. Zhou (eds.).*] Cambridge,
831 United Kingdom and New York, NY, USA: Cambridge University Press. doi:
832 10.1017/9781009157896.009
- 833 Fuhrer, O., Osuna, C., Lapillon, X., Gysi, T., Cumming, B., Bianco, M., ...
834 Schulthess, T. C. (2014, 9). Towards a performance portable, architecture
835 agnostic implementation strategy for weather and climate models. *Super-*
836 *computing Frontiers and Innovations*, 1(1), 44–61. Retrieved from <http://superfri.org/superfri/article/view/17> doi: 10.14529/jsfi140103
- 837 Hartmann, D. L., & Larson, K. (2002, 10). An important constraint on tropical
838 cloud - climate feedback. *Geophysical Research Letters*, 29(20), 12–1. Re-
839 tried from <http://doi.wiley.com/10.1029/2002GL015835> doi: 10.1029/
840 2002GL015835
- 841 Heim, C., Hentgen, L., Ban, N., & Schär, C. (2021). Inter-model Variability in
842 Convection-Resolving Simulations of Subtropical Marine Low Clouds. *Journal*
843 *of the Meteorological Society of Japan. Ser. II*, 99(5), 2021–062. Retrieved
844 from https://www.jstage.jst.go.jp/article/jmsj/99/5/99_2021-062/_article doi: 10.2151/jmsj.2021-062
- 845 Heise, E., Lange, M., Ritter, B., & Schrödin, R. (2003). Improvement and validation
846 of the multilayer soil model. *COSMO Newsletter*, 3, 198–203. Retrieved from
847 <http://www.cosmo-model.org>
- 848 Held, I. M., & Hou, A. Y. (1980, 3). Nonlinear Axially Symmetric Circula-
849 tions in a Nearly Inviscid Atmosphere. *Journal of the Atmospheric Sci-
850 ences*, 37(3), 515–533. Retrieved from [http://journals.ametsoc.org/doi/10.1175/1520-0469\(1980\)037<0515:NASCIA>2.0.CO;2](http://journals.ametsoc.org/doi/10.1175/1520-0469(1980)037<0515:NASCIA>2.0.CO;2) doi:
851 10.1175/1520-0469(1980)037<0515:NASCIA>2.0.CO;2
- 852 Hentgen, L., Ban, N., Kröner, N., Leutwyler, D., & Schär, C. (2019, 4). Clouds
853 in Convection-Resolving Climate Simulations Over Europe. *Journal of*
854 *Geophysical Research: Atmospheres*, 124(7), 3849–3870. Retrieved from
855 <https://onlinelibrary.wiley.com/doi/abs/10.1029/2018JD030150> doi:
856 10.1029/2018JD030150
- 857 Hersbach, H., Bell, B., Berrisford, P., Hirahara, S., Horányi, A., Muñoz-Sabater, J.,
858 ... Thépaut, J. (2020, 7). The ERA5 global reanalysis. *Quarterly Journal*
859 *of the Royal Meteorological Society*, 146(730), 1999–2049. Retrieved from

- 863 <https://onlinelibrary.wiley.com/doi/abs/10.1002/qj.3803>
 864 <https://onlinelibrary.wiley.com/doi/10.1002/qj.3803> doi: 10.1002/qj.3803
- 865 Hohenegger, C., Kornblueh, L., Klocke, D., Becker, T., Cioni, G., Engels, J. F.,
 866 ... Stevens, B. (2020). Climate Statistics in Global Simulations of the
 867 Atmosphere, from 80 to 2.5 km Grid Spacing. *Journal of the Meteorological Society of Japan. Ser. II*, 98(1), 73–91.
 868 Retrieved from www.jstage.jst.go.jp/article/jmsj/98/1/98_2020-005/_article doi:
 869 10.2151/jmsj.2020-005
- 871 Huang, P., Xie, S.-P., Hu, K., Huang, G., & Huang, R. (2013, 5). Patterns of the
 872 seasonal response of tropical rainfall to global warming. *Nature Geoscience*,
 873 6(5), 357–361. Retrieved from <http://www.nature.com/articles/ngeo1792>
 874 doi: 10.1038/ngeo1792
- 875 Huffman, G., E.F. Stocker, D.T. Bolvin, E.J. Nelkin, & Jackson Tan. (2019).
 876 *GPM IMERG Final Precipitation L3 1 day 0.1 degree x 0.1 degree V06*,
 877 Edited by Andrey Savtchenko, Greenbelt, MD, Goddard Earth Sciences Data
 878 and Information Services Center (GES DISC), Accessed: 06.07.2022. doi:
 879 10.5067/GPM/IMERGDF/DAY/06
- 880 Jenney, A. M., Randall, D. A., & Branson, M. D. (2020, 6). Understanding
 881 the Response of Tropical Ascent to Warming Using an Energy Balance
 882 Framework. *Journal of Advances in Modeling Earth Systems*, 12(6). doi:
 883 10.1029/2020MS002056
- 884 Kawai, H., & Shige, S. (2020). Marine Low Clouds and their Parameterization in
 885 Climate Models. *Journal of the Meteorological Society of Japan. Ser. II*, 98(6),
 886 1097–1127. Retrieved from https://www.jstage.jst.go.jp/article/jmsj/98/6/98_2020-059/_article doi: 10.2151/jmsj.2020-059
- 888 Klemp, J. B., & Durran, D. R. (1983, 3). An Upper Boundary Condition Permitting Internal Gravity Wave Radiation in Numerical Mesoscale Models. *Monthly Weather Review*, 111(3), 430–444. Retrieved from [http://journals.ametsoc.org/doi/10.1175/1520-0493\(1983\)111%3C0430:AUBCPI%3E2.0.CO;2](http://journals.ametsoc.org/doi/10.1175/1520-0493(1983)111%3C0430:AUBCPI%3E2.0.CO;2) doi:
 889 10.1175/1520-0493(1983)111%3C0430:AUBCPI%3E2.0.CO;2
- 893 Klemp, J. B., & Wilhelmson, R. B. (1978, 6). The Simulation of Three-Dimensional Convective Storm Dynamics. *Journal of the Atmospheric Sciences*, 35(6), 1070–1096. Retrieved from <http://journals.ametsoc.org/>

- 896 doi/10.1175/1520-0469(1978)035<1070:TSOTDC>2.0.CO;2 doi:
897 10.1175/1520-0469(1978)035<1070:TSOTDC>2.0.CO;2
- 898 Klocke, D., Brueck, M., Hohenegger, C., & Stevens, B. (2017, 12). Rediscovery of
899 the doldrums in storm-resolving simulations over the tropical Atlantic. *Nature
900 Geoscience*, 10(12), 891–896. Retrieved from [http://dx.doi.org/10.1038/
901 s41561-017-0005-4](http://dx.doi.org/10.1038/s41561-017-0005-4) <http://www.nature.com/articles/s41561-017-0005-4>
902 doi: 10.1038/s41561-017-0005-4
- 903 Kriegler, E., Bauer, N., Popp, A., Humpenöder, F., Leimbach, M., Strefler, J., ...
904 Edenhofer, O. (2017, 1). Fossil-fueled development (SSP5): An energy and
905 resource intensive scenario for the 21st century. *Global Environmental Change*,
906 42, 297–315. Retrieved from [https://linkinghub.elsevier.com/retrieve/
907 pii/S0959378016300711](https://linkinghub.elsevier.com/retrieve/pii/S0959378016300711) doi: 10.1016/j.gloenvcha.2016.05.015
- 908 Kröner, N., Kotlarski, S., Fischer, E., Lüthi, D., Zubler, E., & Schär, C. (2017, 5).
909 Separating climate change signals into thermodynamic, lapse-rate and circula-
910 tion effects: theory and application to the European summer climate. *Climate
911 Dynamics*, 48(9-10), 3425–3440. Retrieved from [http://link.springer.com/
912 10.1007/s00382-016-3276-3](http://link.springer.com/10.1007/s00382-016-3276-3) doi: 10.1007/s00382-016-3276-3
- 913 Lau, W. K. M., & Kim, K.-M. (2015, 3). Robust Hadley Circulation changes and in-
914 creasing global dryness due to CO₂ warming from CMIP5 model projections.
915 *Proceedings of the National Academy of Sciences*, 112(12), 3630–3635. Re-
916 tried from <https://pnas.org/doi/full/10.1073/pnas.1418682112> doi:
917 10.1073/pnas.1418682112
- 918 Lau, W. K. M., Kim, K. M., Chern, J. D., Tao, W. K., & Leung, L. R. (2020,
919 1). Structural changes and variability of the ITCZ induced by radia-
920 tion–cloud–convection–circulation interactions: inferences from the Goddard
921 Multi-scale Modeling Framework (GMMF) experiments. *Climate Dynamics*,
922 54(1-2), 211–229. doi: 10.1007/s00382-019-05000-y
- 923 Leutwyler, D., Fuhrer, O., Lapillonne, X., Lüthi, D., & Schär, C. (2016). Towards
924 European-scale convection-resolving climate simulations with GPUs: A study
925 with COSMO 4.19. *Geoscientific Model Development*, 9(9), 3393–3412. doi:
926 10.5194/gmd-9-3393-2016
- 927 Leutwyler, D., & Hohenegger, C. (2021). Weak cooling of the troposphere by
928 tropical islands in simulations of the radiative-convective equilibrium. *Quar-*

- 929 terly *Journal of the Royal Meteorological Society*, 147(736), 1788–1800. doi:
 930 10.1002/qj.3995
- 931 Leutwyler, D., Lüthi, D., Ban, N., Fuhrer, O., & Schär, C. (2017, 5). Evaluation
 932 of the convection-resolving climate modeling approach on continental scales. *Journal of Geophysical Research: Atmospheres*, 122(10), 5237–
 933 5258. Retrieved from <http://doi.wiley.com/10.1002/2016JD026013> doi:
 934 10.1002/2016JD026013
- 935 Li, G., & Xie, S. P. (2014). Tropical biases in CMIP5 multimodel ensemble: The
 936 excessive equatorial pacific cold tongue and double ITCZ problems. *Journal of Climate*, 27(4), 1765–1780. doi: 10.1175/JCLI-D-13-00337.1
- 937 Lin, J. L. (2007, 9). The double-ITCZ problem in IPCC AR4 coupled GCMs:
 938 Ocean-atmosphere feedback analysis. *Journal of Climate*, 20(18), 4497–4525.
 939 doi: 10.1175/JCLI4272.1
- 940 Liu, S., Zeman, C., Sørland, S. L., & Schär, C. (2022). Systematic Calibration of A
 941 Convection-Resolving Model: Application over Tropical Atlantic. *submitted to Journal of Geophysical Research: Atmospheres*.
- 942 Loeb, N. G., Doelling, D. R., Wang, H., Su, W., Nguyen, C., Corbett, J. G., ...
 943 Kato, S. (2018, 1). Clouds and the Earth's Radiant Energy System (CERES)
 944 Energy Balanced and Filled (EBAF) Top-of-Atmosphere (TOA) Edition-
 945 4.0 Data Product. *Journal of Climate*, 31(2), 895–918. Retrieved from
 946 <http://journals.ametsoc.org/doi/10.1175/JCLI-D-17-0208.1> doi:
 947 10.1175/JCLI-D-17-0208.1
- 948 Mechoso, C., Robertson, A., Barth, N., Davey, M., Delecluse, P., Gent, P., ...
 949 Tribbia, J. (1995, 9). The Seasonal Cycle over the Tropical Pacific in Cou-
 950 pled Ocean–Atmosphere General Circulation Models. *Monthly Weather
 951 Review*, 123(9), 2825–2838. doi: 10.1175/1520-0493(1995)123<2825:
 952 TSCOTT>2.0.CO;2
- 953 Nakamura, R., & Mäll, M. (2021, 12). Pseudo Global Warming Sensitivity Exper-
 954 iments of Subtropical Cyclone Anita (2010) Under RCP 8.5 Scenario. *Journal
 955 of Geophysical Research: Atmospheres*, 126(24). doi: 10.1029/2021JD035261
- 956 Noda, A. T., & Satoh, M. (2014). Intermodel variances of subtropical stratocu-
 957 mulus environments simulated in CMIP5 models. , 7754–7761. doi: 10.1002/
 958 2014GL061812.Received

- 962 Ohno, T., Noda, A. T., Seiki, T., & Satoh, M. (2021). Importance of Pressure
963 Changes in High Cloud Area Feedback Due to Global Warming. *Geophysical*
964 *Research Letters*, 48(18). doi: 10.1029/2021GL093646
- 965 Ohno, T., & Satoh, M. (2018). Roles of Cloud Microphysics on Cloud Responses to
966 Sea Surface Temperatures in Radiative-Convective Equilibrium Experiments
967 Using a High-Resolution Global Nonhydrostatic Model. *Journal of Advances in*
968 *Modeling Earth Systems*, 10(8), 1970–1989. doi: 10.1029/2018MS001386
- 969 Ohno, T., Satoh, M., & Noda, A. (2019). Fine Vertical Resolution Radiative-
970 Convective Equilibrium Experiments: Roles of Turbulent Mixing on the
971 High-Cloud Response to Sea Surface Temperatures. *Journal of Advances in*
972 *Modeling Earth Systems*, 11(6), 1637–1654. doi: 10.1029/2019MS001704
- 973 Pichelli, E., Coppola, E., Sobolowski, S., Ban, N., Giorgi, F., Stocchi, P., ...
974 Vergara-Temprado, J. (2021, 6). The first multi-model ensemble of regional
975 climate simulations at kilometer-scale resolution part 2: historical and future
976 simulations of precipitation. *Climate Dynamics*, 56(11-12), 3581–3602. Re-
977 trieval from <https://link.springer.com/10.1007/s00382-021-05657-4>
978 doi: 10.1007/s00382-021-05657-4
- 979 Possner, A., Zubler, E., Fuhrer, O., Lohmann, U., & Schär, C. (2014, 4). A
980 Case Study in Modeling Low-Lying Inversions and Stratocumulus Cloud
981 Cover in the Bay of Biscay. *Weather and Forecasting*, 29(2), 289–304. Re-
982 trieval from <https://journals.ametsoc.org/waf/article/29/2/289/39873/A-Case-Study-in-Modeling-LowLying-Inversions-and> doi:
983 10.1175/WAF-D-13-00039.1
- 985 Prein, A. F., Langhans, W., Fosser, G., Ferrone, A., Ban, N., Goergen, K., ... Le-
986 ung, R. (2015). A review on regional convection-permitting climate modeling:
987 Demonstrations, prospects, and challenges. *Reviews of Geophysics*, 53(2),
988 323–361. Retrieved from <http://dx.doi.org/10.1002/2014RG000475> doi:
989 10.1002/2014RG000475
- 990 Raschendorfer, M. (2001). The new turbulence parameterization of LM. *COSMO*
991 *Newsletter*, 1, 89–97.
- 992 Rasmussen, R., Liu, C., Ikeda, K., Gochis, D., Yates, D., Chen, F., ... Gut-
993 mann, E. (2011, 6). High-Resolution Coupled Climate Runoff Simula-
994 tions of Seasonal Snowfall over Colorado: A Process Study of Current and

- 995 Warmer Climate. *Journal of Climate*, 24(12), 3015–3048. Retrieved from
 996 <http://journals.ametsoc.org/doi/abs/10.1175/2010JCLI3985.1> doi:
 997 10.1175/2010JCLI3985.1
- 998 Reinhardt, T., & Seifert, A. (2006). A three-category ice scheme for LMK. *COSMO*
 999 *Newsletter*, 6, 115–120.
- 1000 Ritter, B., & Geleyn, J.-F. (1992, 2). A Comprehensive Radiation Scheme for Nu-
 1001 matical Weather Prediction Models with Potential Applications in Climate
 1002 Simulations. *Monthly Weather Review*, 120(2), 303–325. Retrieved from
 1003 [http://journals.ametsoc.org/doi/abs/10.1175/1520-0493\(1992\)120%3C0303:ACRSFN%3E2.0.CO;2%5Cnhttp://journals.ametsoc.org/doi/abs/10.1175/1520-0493%281992%29120%3C0303:ACRSFN%3E2.0.CO;2#V5JN_92a2L0.mendeley%5Cnhttp://journals.ametsoc.org/doi/abs/10.1175/1520-0493\(1992\)120%3C0303:ACRSFN%3E2.0.CO;2](http://journals.ametsoc.org/doi/abs/10.1175/1520-0493(1992)120%3C0303:ACRSFN%3E2.0.CO;2%5Cnhttp://journals.ametsoc.org/doi/abs/10.1175/1520-0493%281992%29120%3C0303:ACRSFN%3E2.0.CO;2#V5JN_92a2L0.mendeley%5Cnhttp://journals.ametsoc.org/doi/abs/10.1175/1520-0493(1992)120%3C0303:ACRSFN%3E2.0.CO;2) doi:
 1004 10.1175/1520-0493(1992)120%3C0303:ACRSFN%3E2.0.CO;2#V5JN_92a2L0.mendeley%5Cnhttp://journals.ametsoc.org/doi/abs/10.1175/1520-0493(1992)120%3C0303:ACRSFN%3E2.0.CO;2
- 1005 Rockel, B., Will, A., & Hense, A. (2008, 8). The Regional Climate Model
 1006 COSMO-CLM (CCLM). *Meteorologische Zeitschrift*, 17(4), 347–348. Re-
 1007 trieval from http://www.schweizerbart.de/papers/metz/detail/17/56726/The_Regional_Climate_Model_COSMO_CLM_CCLM?af=crossref doi:
 1008 10.1127/0941-2948/2008/0309
- 1009 Saint-Lu, M., Bony, S., & Dufresne, J. L. (2020). Observational Evidence for a Sta-
 1010 bility Iris Effect in the Tropics. *Geophysical Research Letters*, 47(14). doi: 10
 1011 .1029/2020GL089059
- 1012 Sato, T., Kimura, F., & Kitoh, A. (2007, 1). Projection of global warming onto re-
 1013 gional precipitation over Mongolia using a regional climate model. *Journal of*
 1014 *Hydrology*, 333(1), 144–154. doi: 10.1016/j.jhydrol.2006.07.023
- 1015 Satoh, M., Iga, S. I., Tomita, H., Tsushima, Y., & Noda, A. T. (2012). Response
 1016 of upper clouds in global warming experiments obtained using a global non-
 1017 hydrostatic model with explicit cloud processes. *Journal of Climate*, 25(6),
 1018 2178–2191. doi: 10.1175/JCLI-D-11-00152.1
- 1019 Satoh, M., Stevens, B., Judt, F., Khairoutdinov, M., Lin, S.-j., Putman, W. M.,
 1020 & Düben, P. (2019, 9). Global Cloud-Resolving Models. *Current Climate*
 1021 *Change Reports*, 5(3), 172–184. Retrieved from <http://link.springer.com/10.1007/s40641-019-00131-0> doi: 10.1007/s40641-019-00131-0
- 1022 Schär, C., Frei, C., Lüthi, D., & Davies, H. C. (1996, 3). Surrogate climate-change

- 1028 scenarios for regional climate models. *Geophysical Research Letters*, 23(6),
1029 669–672. Retrieved from <http://doi.wiley.com/10.1029/96GL00265> doi:
1030 10.1029/96GL00265
- 1031 Schär, C., Fuhrer, O., Arteaga, A., Ban, N., Charpiloz, C., Di Girolamo, S., ...
1032 Wernli, H. (2020, 5). Kilometer-scale climate models: Prospects and chal-
1033 lenges. *Bulletin of the American Meteorological Society*, 101(5), E567-E587.
1034 Retrieved from [https://journals.ametsoc.org/bams/article/101/5/
1035 E567/345557/KilometerScale-Climate-Models-Prospects-and](https://journals.ametsoc.org/bams/article/101/5/E567/345557/KilometerScale-Climate-Models-Prospects-and) doi:
1036 10.1175/BAMS-D-18-0167.1
- 1037 Schlemmer, L., Schär, C., Lüthi, D., & Strelbel, L. (2018, 8). A Groundwater and
1038 Runoff Formulation for Weather and Climate Models. *Journal of Advances in
1039 Modeling Earth Systems*, 10(8), 1809–1832. Retrieved from [http://doi.wiley
1040 .com/10.1029/2017MS001260](http://doi.wiley.com/10.1029/2017MS001260) doi: 10.1029/2017MS001260
- 1041 Schneider, T., Teixeira, J., Bretherton, C. S., Brient, F., Pressel, K. G., Schär, C.,
1042 & Siebesma, A. P. (2017). Climate goals and computing the future of clouds.
1043 *Nature Climate Change*, 7(1). doi: 10.1038/nclimate3190
- 1044 Schulz, H., Eastman, R., & Stevens, B. (2021, 9). Characterization and Evolu-
1045 tion of Organized Shallow Convection in the Downstream North Atlantic
1046 Trades. *Journal of Geophysical Research: Atmospheres*, 126(17). doi:
1047 10.1029/2021JD034575
- 1048 Sherwood, S. C., Bony, S., & Dufresne, J.-L. (2014, 1). Spread in model climate
1049 sensitivity traced to atmospheric convective mixing. *Nature*, 505(7481), 37–
1050 42. Retrieved from <http://www.nature.com/articles/nature12829> doi:
1051 10.1038/nature12829
- 1052 Shine, K. P., Bourqui, M. S., de Forster, P. M., Hare, S. H., Langematz, U.,
1053 Braesicke, P., ... Schwarzkopf, M. D. (2003, 4). A comparison of model-
1054 simulated trends in stratospheric temperatures. *Quarterly Journal of the Royal
1055 Meteorological Society*, 129(590 PART A), 1565–1588. doi: 10.1256/qj.02.186
- 1056 Singh, M. S., & O’Gorman, P. A. (2015, 10). Increases in moist-convective up-
1057 draught velocities with warming in radiative-convective equilibrium. *Quar-
1058 terly Journal of the Royal Meteorological Society*, 141(692), 2828–2838. doi:
1059 10.1002/qj.2567
- 1060 Song, X., & Zhang, G. J. (2018, 3). The Roles of Convection Parameterization

- 1061 in the Formation of Double ITCZ Syndrome in the NCAR CESM: I. Atmo-
1062 spheric Processes. *Journal of Advances in Modeling Earth Systems*, 10(3),
1063 842–866. Retrieved from <https://onlinelibrary.wiley.com/doi/10.1002/2017MS001191> doi: 10.1002/2017MS001191
- 1064
1065 Sørland, S. L., Brogli, R., Pothapakula, P. K., Russo, E., Van de Walle, J., Ahrens,
1066 B., ... Thiery, W. (2021, 8). COSMO-CLM regional climate simulations
1067 in the Coordinated Regional Climate Downscaling Experiment (CORDEX)
1068 framework: a review. *Geoscientific Model Development*, 14(8), 5125–5154. Re-
1069 tried from <https://gmd.copernicus.org/articles/14/5125/2021/> doi:
1070 10.5194/gmd-14-5125-2021
- 1071 Stevens, B. (2007, 8). On the Growth of Layers of Nonprecipitating Cumulus Con-
1072 vection. *Journal of the Atmospheric Sciences*, 64(8), 2916–2931. Retrieved
1073 from <http://journals.ametsoc.org/doi/abs/10.1175/JAS3983.1> https://
1074 journals.ametsoc.org/doi/10.1175/JAS3983.1 doi: 10.1175/JAS3983.1
- 1075 Stevens, B., Acquistapace, C., Hansen, A., Heinze, R., Klinger, C., Klocke, D., ...
1076 ZÄNGL, G. (2020). The Added Value of Large-eddy and Storm-resolving
1077 Models for Simulating Clouds and Precipitation. *Journal of the Meteoro-
1078 logical Society of Japan. Ser. II*, 98(2), 395–435. Retrieved from [https://
1079 www.jstage.jst.go.jp/article/jmsj/98/2/98_2020-021/_article](https://www.jstage.jst.go.jp/article/jmsj/98/2/98_2020-021/_article) doi:
1080 10.2151/jmsj.2020-021
- 1081 Stevens, B., Moeng, C.-H., Ackerman, A. S., Bretherton, C. S., Chlond, A., de
1082 Roode, S., ... Zhu, P. (2005, 6). Evaluation of Large-Eddy Simulations via
1083 Observations of Nocturnal Marine Stratocumulus. *Monthly Weather Review*,
1084 133(6), 1443–1462. Retrieved from [http://journals.ametsoc.org/doi/
1085 10.1175/MWR2930.1](http://journals.ametsoc.org/doi/10.1175/MWR2930.1) doi: 10.1175/MWR2930.1
- 1086 Stevens, B., Satoh, M., Auger, L., Biercamp, J., Bretherton, C. S., Chen, X., ...
1087 Zhou, L. (2019, 12). DYAMOND: the DYnamics of the Atmospheric general
1088 circulation Modeled On Non-hydrostatic Domains. *Progress in Earth and
1089 Planetary Science*, 6(1), 61. Retrieved from [https://progearthplanetsci
1090 .springeropen.com/articles/10.1186/s40645-019-0304-z](https://progearthplanetsci.springeropen.com/articles/10.1186/s40645-019-0304-z) doi:
1091 10.1186/s40645-019-0304-z
- 1092 Suhas, E., & Zhang, G. J. (2015). Evaluating convective parameterization closures
1093 using cloud-resolving model simulation of tropical deep convection. *Journal of*

- 1094 *Geophysical Research*, 120(4), 1260–1277. doi: 10.1002/2014JD022246
- 1095 Taylor, K. E., Stouffer, R. J., & Meehl, G. A. (2012, 4). An Overview of CMIP5
1096 and the Experiment Design. *Bulletin of the American Meteorological Society*, 93(4), 485–498. Retrieved from <https://journals.ametsoc.org/doi/10.1175/BAMS-D-11-00094.1> doi: 10.1175/BAMS-D-11-00094.1
- 1097 Tegen, I., Hollrigl, P., Chin, M., Fung, I., Jacob, D., & Penner, J. (1997, 10). Con-
1098 tribution of different aerosol species to the global aerosol extinction optical
1099 thickness: Estimates from model results. *Journal of Geophysical Research
Atmospheres*, 102(20), 23895–23915. doi: 10.1029/97jd01864
- 1100 Tian, B. (2015, 5). Spread of model climate sensitivity linked to double-Intertropical
1101 Convergence Zone bias. *Geophysical Research Letters*, 42(10), 4133–4141. doi:
1102 10.1002/2015GL064119
- 1103 Tsushima, Y., Iga, S.-i., Tomita, H., Satoh, M., Noda, A. T., & Webb, M. J. (2014,
1104 9). High cloud increase in a perturbed SST experiment with a global non-
1105 hydrostatic model including explicit convective processes. *Journal of Ad-
1106 vances in Modeling Earth Systems*, 6(3), 571–585. Retrieved from <http://doi.wiley.com/10.1002/2013MS000301> doi: 10.1002/2013MS000301
- 1107 Vergara-Temprado, J., Ban, N., Panosetti, D., Schlemmer, L., & Schär, C. (2020,
1108 3). Climate Models Permit Convection at Much Coarser Resolutions Than
1109 Previously Considered. *Journal of Climate*, 33(5), 1915–1933. Retrieved
1110 from <http://journals.ametsoc.org/doi/10.1175/JCLI-D-19-0286.1> doi:
1111 10.1175/JCLI-D-19-0286.1
- 1112 Vial, J., Bony, S., Dufresne, J., & Roehrig, R. (2016, 12). Coupling between lower-
1113 tropospheric convective mixing and low-level clouds: Physical mechanisms and
1114 dependence on convection scheme. *Journal of Advances in Modeling Earth Sys-
1115 tems*, 8(4), 1892–1911. Retrieved from <https://onlinelibrary.wiley.com/doi/abs/10.1002/2016MS000740> doi: 10.1002/2016MS000740
- 1116 Vial, J., Bony, S., Stevens, B., & Vogel, R. (2017). Mechanisms and Model Diversity
1117 of Trade-Wind Shallow Cumulus Cloud Feedbacks: A Review. *Surveys in Geo-
1118 physics*, 38(6), 1331–1353. doi: 10.1007/s10712-017-9418-2
- 1119 von Storch, J.-S., Putrasahan, D., Lohmann, K., Gutjahr, O., Jungclaus, J.,
1120 Bittner, M., ... Roeckner, E. (2017). *MPI-M MPIESM1.2-HR model
output prepared for CMIP6 HighResMIP*. Earth System Grid Federa-
- 1121 1122 1123 1124 1125 1126

- tion. Retrieved from <https://doi.org/10.22033/ESGF/CMIP6.762> doi: 10.22033/ESGF/CMIP6.762
- Waliser, D. E., & Gautier, C. (1993, 11). A Satellite-derived Climatology of the ITCZ. *Journal of Climate*, 6(11), 2162–2174. Retrieved from [http://journals.ametsoc.org/doi/10.1175/1520-0442\(1993\)006<2162:ASDCOT>2.0.CO;2](http://journals.ametsoc.org/doi/10.1175/1520-0442(1993)006<2162:ASDCOT>2.0.CO;2) doi: 10.1175/1520-0442(1993)006<2162:ASDCOT>2.0.CO;2
- Warren, S., Hahn, C., London, J., Chervin, R., & Jenne, R. (1988, 12). *Global distribution of total cloud cover and cloud type amounts over the ocean* (Tech. Rep.). USDOE Office of Energy Research (ER). Retrieved from <http://www.osti.gov/servlets/purl/5415329-XbAE7q/> doi: 10.2172/5415329
- Webb, M. J., Andrews, T., Bodas-Salcedo, A., Bony, S., Bretherton, C. S., Chadwick, R., ... Watanabe, M. (2017). The Cloud Feedback Model Intercomparison Project (CFMIP) contribution to CMIP6. *Geoscientific Model Development*, 10(1). doi: 10.5194/gmd-10-359-2017
- Webb, M. J., & Lock, A. P. (2020, 9). Testing a Physical Hypothesis for the Relationship Between Climate Sensitivity and Double-ITCZ Bias in Climate Models. *Journal of Advances in Modeling Earth Systems*, 12(9), 4133–4141. Retrieved from <https://onlinelibrary.wiley.com/doi/10.1029/2019MS001999> doi: 10.1029/2019MS001999
- Wicker, L. J., & Skamarock, W. C. (2002, 8). Time-Splitting Methods for Elastic Models Using Forward Time Schemes. *Monthly Weather Review*, 130(8), 2088–2097. Retrieved from [https://doi.org/10.1175/1520-0493\(2002\)130%3C2088:TSMFEM%3E2.0.CO;2](https://doi.org/10.1175/1520-0493(2002)130%3C2088:TSMFEM%3E2.0.CO;2) doi: 10.1175/1520-0493(2002)130%3C2088:TSMFEM%3E2.0.CO;2
- Wing, A. A., Stauffer, C. L., Becker, T., Reed, K. A., Ahn, M. S., Arnold, N. P., ... Zhao, M. (2020). Clouds and Convective Self-Aggregation in a Multimodel Ensemble of Radiative-Convective Equilibrium Simulations. *Journal of Advances in Modeling Earth Systems*, 12(9), 1–38. doi: 10.1029/2020MS002138
- Wodzicki, K. R., & Rapp, A. D. (2016). Long-term characterization of the Pacific ITCZ using TRMM, GPCP, and ERA-Interim. *Journal of Geophysical Research*, 121(7), 3153–3170. doi: 10.1002/2015JD024458
- Wood, R. (2012, 8). Stratocumulus Clouds. *Monthly Weather Review*, 140(8), 2373–2423. Retrieved from <http://journals.ametsoc.org/doi/abs/10.1175>

- 1160 MWR-D-11-00121.1`https://journals.ametsoc.org/mwr/article/140/8/`
1161 2373/71595/Stratocumulus-Clouds doi: 10.1175/MWR-D-11-00121.1
- 1162 Wu, W., & Lynch, A. H. (2000, 9). Response of the seasonal carbon cycle in high
1163 latitudes to climate anomalies. *Journal of Geophysical Research: Atmospheres*,
1164 105(D18), 22897–22908. doi: 10.1029/2000JD900340
- 1165 Zelinka, M. D., Randall, D. A., Webb, M. J., & Klein, S. A. (2017, 10). Clear-
1166 ing clouds of uncertainty. *Nature Climate Change*, 7(10), 674–678. Re-
1167 tried from `http://www.nature.com/articles/nclimate3402` doi:
1168 10.1038/nclimate3402
- 1169 Zelinka, M. D., Zhou, C., & Klein, S. A. (2016, 9). Insights from a refined decompo-
1170 sition of cloud feedbacks. *Geophysical Research Letters*, 43(17), 9259–9269. Re-
1171 tried from `http://doi.wiley.com/10.1002/2016GL069917` doi: 10.1002/
1172 2016GL069917
- 1173 Zeman, C., Wedi, N. P., Dueben, P. D., Ban, N., & Schär, C. (2021, 7). Model
1174 intercomparison of COSMO 5.0 and IFS 45r1 at kilometer-scale grid spac-
1175 ing. *Geoscientific Model Development*, 14(7), 4617–4639. doi: 10.5194/
1176 gmd-14-4617-2021
- 1177 Zhang, G. J., Song, X., & Wang, Y. (2019, 11). The double ITCZ syndrome in
1178 GCMs: A coupled feedback problem among convection, clouds, atmospheric
1179 and ocean circulations. *Atmospheric Research*, 229(December 2018), 255–
1180 268. Retrieved from `https://doi.org/10.1016/j.atmosres.2019.06`
1181 .023`https://linkinghub.elsevier.com/retrieve/pii/S0169809518316788`
1182 doi: 10.1016/j.atmosres.2019.06.023
- 1183 Zhou, W., Leung, L. R., Lu, J., Yang, D., & Song, F. (2020, 11). Contrasting Re-
1184 cent and Future ITCZ Changes From Distinct Tropical Warming Patterns.
1185 *Geophysical Research Letters*, 47(22). doi: 10.1029/2020GL089846
- 1186 Zuidema, P., Redemann, J., Haywood, J., Wood, R., Piketh, S., Hipondoka, M.,
1187 & Formenti, P. (2016, 7). Smoke and Clouds above the Southeast Atlantic:
1188 Upcoming Field Campaigns Probe Absorbing Aerosol's Impact on Climate.
1189 *Bulletin of the American Meteorological Society*, 97(7), 1131–1135. Retrieved
1190 from `https://journals.ametsoc.org/doi/10.1175/BAMS-D-15-00082.1`
1191 doi: 10.1175/BAMS-D-15-00082.1